國立臺灣大學工學院化學工程學系

碩士論文

Department of Chemical Engineering

College of Engineering

National Taiwan University

Master's Thesis

功能性金屬有機框架材料於雙模態光聲影像與電腦斷層掃描之應用

Functional Medal-Organic Frameworks for Dual-Modal Photoacoustic and Computed Tomography Imaging Applications

陳彥璋

Yen-Chang Chen

指導教授: 吳嘉文 博士

Advisor: Kevin C.-W. Wu, Ph.D.

中華民國 114 年 7 月

July 2025

doi:10.6342/NTU202501342

國立臺灣大學碩士學位論文
口試委員會審定書
MASTER'S THESIS ACCEPTANCE CERTIFICATE
NATIONAL TAIWAN UNIVERSITY

功能性金屬有機框架材料於雙模態光聲影像與電腦斷層掃描之應用

Functional Metal-Organic Frameworks for Dual-Modal Photoacoustic and Computed Tomography Imaging Applications

本論文係 陳彥璋 (R12524050) 在國立臺灣大學化學工程學系完成之碩士學位論文，於民國 114 年 6 月 23 日承下列考試委員審查通過及口試及格，特此證明。

The undersigned, appointed by the Department / Graduate Institute of Chemical Engineering on 23th June 2025 have examined a Master's Thesis entitled above presented by Yen-Chang, Chen (R12524050) candidate and hereby certify that it is worthy of acceptance.

口試委員 Oral examination committee:

（指導教授 Advisor）

系（所、學位學程）主管 Director:

致謝

轉眼間已經在台灣大學化工系待了六年了，四年的大學生活，緊接著是兩年的研究生生活，感慨之餘也要謝謝在這一路上陪伴與支持我的大家。

首先，感謝吳嘉文老師一路上的教導與支持，給予我許多的資源，我也在老師身上學習到很多課堂上學習不到的知識，老師對學生的包容與大方，我想是許多實驗室無可比擬的。其次，我要感謝我的父母，在我求學階段不吝嗇的給予我資源以及支持我的想法，讓我有自由且又充裕的發展空間。再來要感謝的是我的女朋友瑀康，從升碩一的暑假認識後，到交往，一路上對我呵護與陪伴，使我感受到前所未有的溫暖，也使我變得更好更好，陪著我一起進步，也在我低潮的時候讓我明白我不是一個人。接著我要感謝從我進實驗室以來一直照顧我的學長姐，從在水源認識的博修、楚仁、柏群、明峰、崇慧，鄭江凝態的子茗、子榕、振杰、彭彭、松柏、Philip、Ed、Sagar、威盛、子芸、明柔、偉哲，再到國衛院的淑萍以及祐陞，沒有祐陞的教導也不會有這篇論文，在實驗上真的學到了非常非常多。接著要感謝在國衛院的夥伴文哲給予的幫助和陪伴，以及在實驗室幫助我許多忙和陪我聊天的在萱、倢伃、顗平、偉庭再來要感謝也被我視為學長等級的學弟侑嘉給予我很多的幫助。最後，感謝所有實驗室夥伴的幫助，特別是翔佑、泳怡、邱鴻、欣昱、敬庭、Wu San、Miya、宜絹、芷欣、成寬、青秀等等。除了實驗室夥伴之外也要謝謝水源卓越大樓 12 樓的實驗室、鄭江樓、以及碩一經常陪我到三點的凝態實驗室和 BOT 宿舍、還有常常讓我看到日出，像此刻打字的當下的國衛院及國衛院宿舍，阿還有半夜給我能量的國衛院販賣機。除此之外，也謝謝我的碩士口試的委員鍾仁傑教授、游佳欣教授、莊爾元教授，使我的論文更加完整。最後謝謝同步輻射、生技園區提供的儀器服務、台大積學館、也謝謝系上行政及儀器人員許多的幫忙。要感謝的人實在太多，沒辦法全部一一列出。

總之這一路上沒有你們，就不會有如今的我。再用一次 If without imaging, medicine is blind, and without everyone, I would be blind.

doi:10.6342/NTU202501342

中文摘要

非侵入式癌症影像技術能夠提供結構與功能層面的腫瘤綜合資訊，進而提升診斷準確性。本研究中，我們開發了負載鈀奈米顆粒的基於鉿金屬有機框架（Hf-EDB）材料，即 Pd@Hf-EDB，作為高效的電腦斷層掃描（CT）與光聲影像（PAI）雙模態顯影劑。Pd@Hf-EDB 的優異表現來自於三方面的協同作用：(i) 含高原子序元素鉿的 MOF 具備卓越的 X 光吸收能力；(ii) H_2EDB 有機配體具有特殊的 π 供體與 π 受體特性，能夠強力錨定貴金屬；(iii) 鈀奈米顆粒則因強烈的能帶間躍遷，在紫外到近紅外區域具有寬廣的吸收範圍。透過 X 光繞射（XRD）、掃描式電子顯微鏡（SEM）、穿透式電子顯微鏡（TEM）、動態光散射（DLS）與能量散射 X 光光譜（EDS）等分析技術，成功證實了 Pd@Hf-EDB 奈米粒子的合成。軟 X 光斷層掃描（SXT）結果進一步驗證了 Pd@Hf-EDB 能夠經由胰臟癌細胞株 BxPC-3 細胞的吞噬作用進入細胞。體外實驗顯示，Pd@Hf-EDB 在 CT 成像中的表現優於傳統分子型對比劑（如 Iohexol）。此外，Pd@Hf-EDB 在紫外-可見-近紅外區域展現出廣泛的吸收範圍，且相較於金奈米棒（GNRs），在光聲影像方面具有更優異的性能。進一步透過活體異種移植腫瘤模型實驗，證實了 Pd@Hf-EDB 於腫瘤區域產生明顯的對比增強，展現其在 PAI 與 CT 影像的卓越應用潛力。

關鍵字：顯影劑、電腦掃描斷層、光聲影像、雙模態影像、金屬有機框架、孔洞材料、奈米材料。

doi:10.6342/NTU202501342

Abstract

Noninvasive cancer imaging improves diagnostics by providing comprehensive information on structural and functional tumors. Herein, we explored palladium nanoparticles loaded hafnium-based metal-organic framework (Hf-EDB) i.e., Pd@Hf-EDB as an efficient dual modal contrast agent for computed tomography (CT) and photoacoustic imaging (PAI). The synergistic collaborations between (i) high-Z element Hf based MOF with superior X-rays absorbing capabilities, (ii) H_2EDB linkers with special π-donation and π-acceptor characteristics capable of strongly anchoring noble metals and (iii) Pd nanoparticles with broad absorption in the UV to NIR regions due to strong interband transition; are ideal for implementation in CT and PAI. The successful synthesis of Pd@Hf-EDB nanoparticles were confirmed through morphology, crystallinity, and compositional characterizations using XRD, SEM, TEM, DLS, and EDS. Soft X-ray tomography (SXT), verified cellular uptake via phagocytosis of Pd@Hf-EDB by BxPC-3 tumor cells. In-vitro experiments revealed superior CT imaging performance of Pd@Hf-EDB over traditional molecular contrast agents like Iohexol. Broad absorption range in the UV-Vis/NIR regions and superior PAI capabilities of Pd@Hf-EDB relative to gold nanorods (GNRs) is reported. Furthermore, the in vivo xenograft model demonstrated significant contrast enhancements near the tumor highlighting the excellent PAI and CT capabilities of the synthesized Pd@Hf-EDB.

doi:10.6342/NTU202501342

Keywords: *contrast agent, computed tomography, photoacoustic imaging, dual-modal imaging, metal-organic frameworks, porous materials, nanomaterials*.

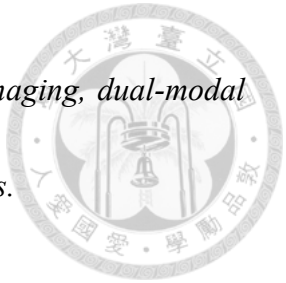

doi:10.6342/NTU202501342

Table of Contents

口試委員會審定書 i

致謝 ii

中文摘要 iii

Abstract iv

Table of Contents vi

List of Figures viii

List of Tables xii

1. Introduction 1

1.1. Introduction from Published Work 1
1.2. Importance of Cancer Imaging in Early Diagnosis 6
1.3. Principles and Limitations of Computed Tomography (CT) 6
1.4. Advantages of Photoacoustic Imaging and Complementarity to CT 7
1.5. Mechanism and Contrast Agents of Photoacoustic Imaging 9
1.6. Design Strategy for Dual-Modal CT/PA Imaging Agents 10
1.7. Research Objective 12

2. Experimental section 13

2.1. Materials 13
2.2. Synthesis of 4,4'- (ethyne-1,2-diyl) dibenzoic acid (H_2EDB) Linker 18
2.2.1 Synthesis of Me_2EDB 19
2.2.2 Synthesis of H_2EDB 20
2.3. Synthesis of Hf-EDB 20
2.4. Incorporation of Pd NPs in Hf-EDB 21
2.5. Synthesis of Gold Nanorods 23
2.6. Characterization 23
2.6.1 Scanning Electron Microscopy (SEM) 23

doi:10.6342/NTU202501342

2.6.2 X-ray Diffraction (XRD) 24
2.6.3 Zeta Potential 24
2.6.4 Particle Size 24
2.6.5 Specific Surface Area 25
2.6.6 Nuclear Magnetic Resonance (NMR) 25
2.6.7 Transmission Electron Microscope (TEM) 25
2.6.8 Inductively coupled plasma optical emission spectrometer (ICP-OES) 26
2.6.9 Ultraviolet-visible (UV-Vis) 26
2.7. Cell Line 26
2.8. Cell Subculture 26
2.9. Cell Viability 27
2.10. Observing the Cellular Uptake of Pd@Hf-EDB using SXT. 28
2.11. In vitro CT imaging 30
2.12. In vitro PA imaging 31
2.13. Animal Model 32

3. Results and Discussion 34

3.1. Synthesis and Characterization of H_2EDB Linker 34
3.2. Synthesis and Characterization of Hf-EDB nanoparticles 37
3.3. Incorporation of Pd NPs and Characterization of Pd@Hf-EDB nanoparticles. 40
3.4. Cell Viability 48
3.5. Observing the Cellular Uptake of Pd@Hf-EDB using SXT 49
3.6. In vitro CT imaging 54
3.7. In vitro PA imaging 58
3.8. In vivo PA imaging 64
3.9. Comparative analysis with leading technologies 66
3.10. Study limitations 70

4. Conclusions 74

5. References 76

Appendix 83

doi:10.6342/NTU202501342

List of Figures

Figure 1.1. Schematic illustration of the development of Pd@Hf-EDB as a dual-modal contrast agent for photoacoustic imaging and computed tomography. 5

Figure 2.1. Synthesis of H_2EDB: (a) Preparing Me_2EDB through Sonogashira Cross-Coupling, (b) Hydrolysis of the Me_2EDB to form H_2EDB. 19

Figure 2.2. Synthesis of the Pd@Hf-EDB 22

Figure 2.3 Mechanism of the AlamarBlue assay 28

Figure 2.4. The detail of the AlamarBlue assay experiment 28

Figure 3.1. Nuclear magnetic resonance (NMR) spectra. (a) NMR ^1H spectrum of Me_2EDB, with $CDCl_3$ as the solvent, (b) NMR ^1H spectrum of H_2EDB, with DMSO-d_6 used as the solvent. 36

Figure 3.2. The NMR ^{13}C spectrum of the H_2EDB, with DMSO-d_6 used as the solvent. 37

Figure 3.3. Characterization of Hf-EDB nanoparticles. (a) XRD patterns of Hf-EDB, (b) Size distribution of Hf-EDB obtained from DLS measurements with four batches (n = 4), (c) SEM image of Hf-EDB with low magnification, (d) SEM image of Hf-EDB with high magnification. 38

Figure 3.4. Characterization of Pd@Hf-EDB nanoparticles. (a) SEM image of Pd@Hf-EDB, (b) Size distribution of Pd@Hf-EDB obtained from DLS

doi:10.6342/NTU202501342

measurements with four batches (n = 4), (c) N_2 adsorption and desorption isotherms of Hf-EDB and Pd@Hf-EDB, (d) Hydrodynamic size of Pd@Hf-EDB dispersed in different media at different storage time, (e) Cell viability of BxPC-3 cells treated with Hf-EDB and Pd@Hf-EDB, (f) Cell viability of RAW 264.7 cells treated with Hf-EDB and Pd@Hf-EDB. 42

Figure 3.5. Percentage of original Hf and Pd content remaining in the supernatants of Pd@Hf-EDB (1 mg/mL) after being stored at 37 °C for 7 days. 44

Figure 3.6. (a) HR-TEM image of Pd@Hf-EDB, (b)EDS mapping results of Pd@Hf-EDB 46

Figure 3.7. Lattice fringes of the Pd nanoparticles inside the Hf-EDB. 47

Figure 3.8. (a) The absorbance spectra of Hf-EDB and Pd@Hf-EDB. (b) The absorbance spectra of Pd@Hf-EDB dispersed in water at different concentrations. 48

Figure 3.9. The Cellular Uptake of Pd@Hf-EDB in Soft X-ray Tomography (SXT) (a) SXT and cryo-fluorescence microscopy of the BxPC-3 cells phagocytosed Pd@Hf-EDB. The cell nucleus, mitochondria, and acidic compartment are stained by Hoechst 33342, MitoTracker, and LysoTracker, respectively. (b) The Z-stack SXT image was reconstructed into 200 slices. Arrow: Pd@Hf-EDB. 51

doi:10.6342/NTU202501342

Figure 3.10. SXT and cryo-fluorescence microscopy of the BxPC-3 cells phagocytosed Pd@Hf-EDB. 52

Figure 3.11. SXT and cryo-fluorescence microscopy of the BxPC-3 cells phagocytosed Pd@Hf-EDB. 52

Figure 3.12. SXT and cryo-fluorescence microscopy of the BxPC-3 cells without Pd@Hf-EDB. 53

Figure 3.13. (a) In vitro phantom CT contrast images of Hf-EDB, iohexol, and Pd@Hf-EDB at different concentrations: 0, 2.5, 5, 10, 20 mg/mL. (b) CT values of Hf-EDB, iohexol, and Pd@Hf-EDB at different concentrations: 0, 2.5, 5, 10, and 20 mg/mL. 56

Figure 3.14. *In vitro* PA imaging of Pd@Hf-EDB nanoparticles. (a) Absorbance spectra of Pd@Hf-EDB dispersed in water at different concentrations. (b) The absorbance of Pd@Hf-EDB to varying concentrations for λ = 750, 800, 850, 900, 950, 975 nm. (c) PA signal of Pd@Hf-EDB and GNRs for different optical densities at 800 nm. (d) PA signal and absorbance of Pd@Hf-EDB at 100 ppm for different wavelengths. (e) In vitro model scheme for simulating blood vessels. (f) PA signal of Pd@Hf-EDB and GNRs at 100 ppm for different wavelengths. 59

Figure 3.15. *In vivo* PA performance of Pd@Hf-EDB nanoparticles. (a) Ultrasound

doi:10.6342/NTU202501342

images of the BxPC-3 cells in the xenografted tumor in the nude mice. (b) A 3D sectional view of the PA images of the tumor at different positions post-injection of Pd@Hf-EDB. (c) A 3D sectional view of the CT images of the tumor at different positions post-injection of Pd@Hf-EDB..... 65

doi:10.6342/NTU202501342

List of Tables

Table 2.1. Materials 14

Table 3.1. Hydrodynamic Size and PDI of Hf-EDB and Pd@Hf-EDB 40

Table 3.2. Metal weight percent and ζ-potential of Hf-EDB and Pd@Hf-EDB 43

Table 3.3. Extinction coefficients at different wavelengths 60

Table 3.4. Comparative analysis of Pd@Hf-EDB with leading imaging technologies 69

Table 3.5. Comparative analysis of Pd@Hf-EDB with other dual-modal imaging materials 69

doi:10.6342/NTU202501342

1. Introduction

1.1. Introduction from Published Work

Noninvasive cancer imaging aimed at providing structural and functional information about tumors has become essential in clinical care as it can significantly improve diagnostic accuracy.[1-4] Noninvasive imaging substantially lowers the risk of complications by reducing unnecessary surgical procedures, enhancing patient comfort, and developing personalized treatment(s).[4-6] Recently, noninvasive imaging techniques, including PET[7, 8], MRI[9], CT[10], SPECT[11], and ultrasound[12, 13] are extensively utilized in clinical practice. Driven by an ever-increasing need for improvements in reliability and accuracy newer technologies have emerged including PAI[14]. As such, different imaging modalities possessing unique combinations of capabilities and functions, are developed and tailored to suit specific conditions. Many contrast agents with multimodal imaging capabilities are being investigated to harness the advantages of various imaging techniques and overcome the limitations of single-modality imaging. For instance, Cai et al.[15] reported on a dual-function PET and near-infrared fluorescence probe for tumor vasculature imaging. Zhang et al.[16] developed Gd/CuS-loaded nanogels to enable MR/PA dual-mode imaging-guided photothermal therapy. Song et al.[17] investigated multimodal image fusion methods using MRI and PET to improve Alzheimer's disease

doi:10.6342/NTU202501342

diagnosis. Conclusively, multimodal imaging approach offers several benefits, such as obtaining complementary diagnostic information at the benefit of reduced dosage and frequency of contrast agent use.[15, 18, 19]

CT is a widely used diagnostic tool that provides detailed cross-sectional images of the body and high-resolution anatomical information with rapid imaging capabilities.[20] CT relies on the differential absorption of X-rays by various tissues, often using contrast agents to enhance image quality.[20, 21] On the other hand, PAI is a relatively new imaging modality that combines the high contrast of optical imaging with the high spatial resolution of ultrasound.[22-25] PAI utilizes the PA effect when an optical absorber such as hemoglobin is induced by a laser pulse, causing thermoelastic expansion thereby generating ultrasound waves (PA signals) that can be detected to form optical images.[26, 27] A significant advantage of PAI in tumor imaging is its ability to provide functional and molecular information on the tissues,[28] such as tumor angiogenesis[29] and hypoxia in various types of tumors.[13, 30] Furthermore, imaging in the near-infrared range, allows deeper tissue penetration and reduces scattering, making it ideal for in-depth imaging of body structures.[24, 31, 32] However, PA capability is inherently limited by the blood supply around the tumor, particularly for small or poorly vascularized early tumors. Thus, the

doi:10.6342/NTU202501342

use of contrast agents can provide more functional and molecular information, improving the accuracy and complexity of tumor monitoring.[28, 33] To this end, nanoparticles are well suited for designing multi-modal contrast agents due to their excellent potential for functionalization.[34, 35] They can effectively combine diverse and specialized properties from different materials to produce desired aptitudes including enhanced imaging capabilities and therapeutic applications.

Consequently, nanomaterial augmented dual-modal contrast agents capable of harnessing the advantages of both CT and PAI techniques such agents have been reported in recent years. For instance, Orza et al. developed Au-Agl nanocomposite as a dual-modal contrast agent which could simultaneously enhance both CT and PA imaging.[36] Additionally, highly porous materials such as metal-organic frameworks (MOFs) composed of metal clusters and organic linkers are exceptionally apt as proficient nanocarriers. MOFs owing to unique advantageous properties including high porosity, tunable pore size, and surface functionalities can be efficiently tailored to meet the ideal characteristics for imaging contrast agents and delivering drugs.[37-39] They are constructed via coordination bonds between various metal ions or secondary building units (SBUs) and organic ligands, allowing for the formation of different MOFs.

doi:10.6342/NTU202501342

In this work, we developed a novel dual-modal contrast agent for CT and PAI, by combining Pd nanoparticles and Hf-based MOF. Hf-based MOF (Hf-EDB) composed of $Hf_6O_4(OH)_4$ clusters and 4,4'-(ethyne-1,2-diyl) di-benzoic acid (H_2EDB) linker was strategically chosen as the nanocarrier. The Hf is a high-Z element, which can absorb more X-rays than soft tissue. Consequently, when precisely accumulated in the tumor site, will have a higher contrast for X-ray than the healthy tissue, thus functioning as a good CT contrast agent. Furthermore, the ethynyl groups on the H_2EDB linkers have special π-donation and π-acceptor characteristics that can strongly interact with the noble metal ions.[40] Previously, we have reported that Pd^{2+} can adsorb to the ethynyl groups from other linkers in the pores of Hf-PEB and reduce them into Pd nanoparticles (Pd NPs).[41] Pd NPs can be effectively loaded into the pores of Hf-EDB in the same way to produce Pd@Hf-EDB. Moreover, these loaded Pd nanoparticles exhibit strong interband transition absorption that provides a broad absorption from the UV to NIR regions,[42] enabling them to be ideal contrast agent for PAI in NIR regions. Compared to traditional molecular contrast agents, metallic nanoparticles offer several advantages.[35, 43, 44] These nanoparticles generally have longer circulation times, higher stability, and can achieve the same imaging effect at lower doses when used in vivo.[35, 45] Their ease of functionalization is extremely beneficial for targeted imaging, providing excellent sensitivity and specificity. In particular, traditional iodine-based contrast agents

doi:10.6342/NTU202501342

employed for CT have limitations including short circulation time and potential nephrotoxicity, which is a concern for patients with pre-existing kidney conditions.[46-48] Therefore, we demonstrated that the synthesized Pd@Hf-EDB possessed dual-modal imaging capacities. It exhibited higher X-ray absorbance than iodine-based contrast agents and possessed superior imaging capabilities as compared to gold nanorods (GNRs) owing to Pd nanoparticles with stability than GNRs after long-term laser irradiation.[18] These results show that Pd@Hf-EDB possesses excellent imaging capabilities for both CT and PAI. The overall experimental concept is schematically illustrated in Figure 1.1.

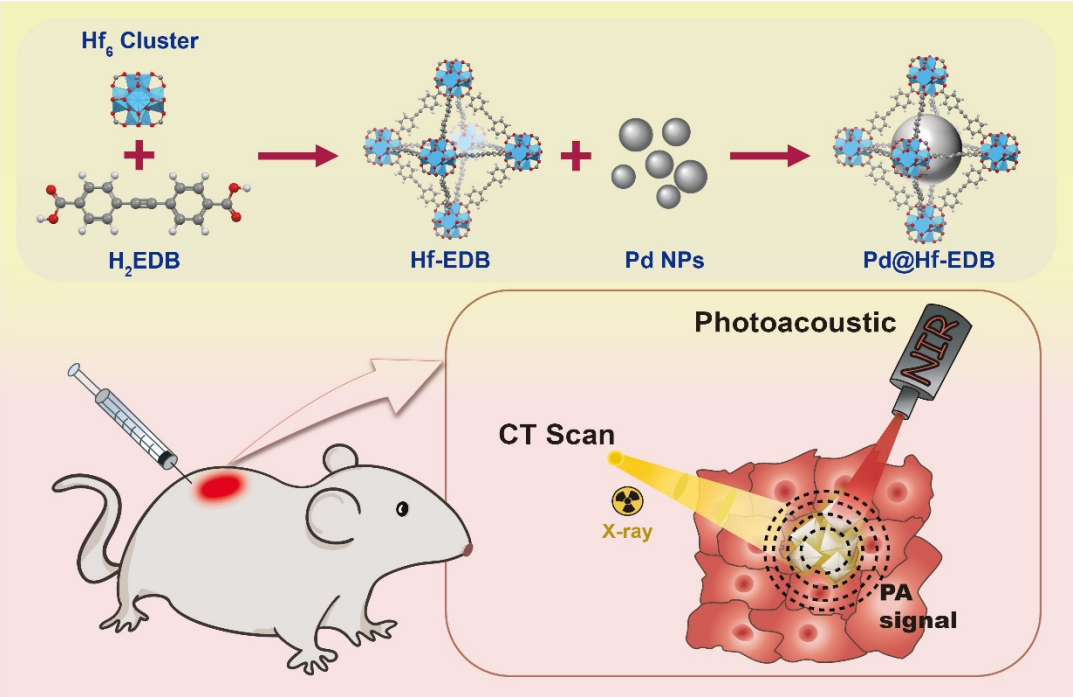

Figure 1.1. Schematic illustration of the development of Pd@Hf-EDB as a dual-modal contrast agent for photoacoustic imaging and computed tomography.

doi:10.6342/NTU202501342

1.2. Importance of Cancer Imaging in Early Diagnosis

Cancer has become one of the most serious threats to global public health. According to the International Agency for Research on Cancer (IARC), the number of new cancer cases in 2050 is expected to increase by around 75% compared to 2022. Cancer-related deaths are also likely to continue rising. Detecting cancer at an early stage is crucial to improving patient survival, and this largely depends on the effectiveness of imaging techniques. For example, in early-stage pancreatic cancer, there are usually no obvious symptoms. Without medical imaging, early diagnosis is nearly impossible; with imaging, the cancer can be found and treated in time. In the case of pancreatic cancer, early detection and intervention can improve the 5-year survival rate from about 3% to as high as 44%. Imaging also plays a pivotal role in precision medicine, as the saying goes, “Without imaging, medicine is blind.”

1.3. Principles and Limitations of Computed Tomography (CT)

Computed tomography (CT) is widely used in cancer imaging because it offers high spatial resolution, rapid image acquisition, and is relatively accessible at a reasonable cost. However, to distinguish tumors from normal tissue on CT scans, contrast agents are essential for enhancing the differences in X-ray absorption. CT contrast agents can be

doi:10.6342/NTU202501342

categorized into two main types: (1) Molecular contrast agents: Typically, iodine-based compounds, which are the most common commercially used CT contrast agents. (2) Nanoparticle contrast agents: Nanoparticles containing high atomic number (high-Z) elements are an emerging alternative. They tend to circulate longer, produce stronger X-ray attenuation, and offer greater stability in vivo compared to molecular agents. These properties make nanoparticle-based agents a compelling subject of study for improved CT imaging.

In our study, we selected a hafnium-based metal-organic framework (Hf-EDB) as the CT contrast agent platform. Hf is a high-Z element that provides strong X-ray absorption, and MOFs offer a versatile nanostructure for further functionalization. This choice was made to leverage the advantages of nanoparticle-based contrast while maintaining a small particle size and good colloidal stability.

1.4. Advantages of Photoacoustic Imaging and Complementarity to CT

While CT is a powerful diagnostic tool, it has several limitations:(1) High contrast dose requirement: Achieving clear images often requires a high dose of iodine-based contrast agent, which can burden patients and increase the risk of side effects. (2) Lack

doi:10.6342/NTU202501342

of functional information: CT primarily provides anatomical details and does not reveal functional information about the tumor. (3) Single snapshot imaging: CT scans are typically used as one-time or infrequent diagnostics, making it difficult to perform continuous or real-time monitoring of dynamic processes.

To address these limitations, we introduce photoacoustic (PA) imaging as a complementary modality to CT. In contrast to CT, PA imaging can provide functional insights and real-time tracking while potentially reducing the required dose of contrast agent. Specifically, PA imaging offers: (1) Functional and molecular information: For instance, PA imaging can visualize tumor angiogenesis and vascular distribution, giving insight into tumor biology that CT alone cannot provide. (2) Reduced contrast usage: PA signals can be strong with inherently present chromophores such as hemoglobin. PA contrast agents can be used at lower doses than CT agents to achieve sufficient imaging contrast. (3) Real-time tracking capability: PA imaging can be performed repeatedly or even continuously in a relatively safe manner, allowing monitoring of dynamic changes in tumors over time.

doi:10.6342/NTU202501342

Therefore, combining CT and PA imaging in a dual-modal approach could harness the strengths of each modality. The goal of our research is to develop a CT/PA dual-modal contrast agent that enables high quality anatomical imaging from CT alongside functional from PA, thereby overcoming CT's shortcomings and improving overall diagnostic accuracy.

1.5. Mechanism and Contrast Agents of Photoacoustic Imaging

PA imaging is a hybrid imaging technique that combines optical illumination with ultrasonic detection to produce high contrast images of tissue. The principle of PA imaging can be summarized as follows: A pulsed laser illuminates the tissue. The light energy is absorbed by adsorption material in the tissue. The absorbed optical energy causes a rapid local temperature rise, leading to thermoelastic expansion of the tissue. This expansion generates ultrasonic pressure waves known as the photoacoustic effect. Ultrasound transducers detect these photoacoustic waves, and the signals are processed to reconstruct an image of the optical absorption distribution in the tissue.

doi:10.6342/NTU202501342

Using near-infrared (NIR) light in PA imaging is advantageous because NIR wavelengths penetrate deeper into biological tissues with less scattering, enabling imaging several centimeters below the surface. PA imaging therefore provides high optical contrast since it relies on optical absorption properties with the good spatial resolution of ultrasound imaging. Many types of contrast agents have been explored to enhance PA imaging, especially to target specific molecular features or to boost signals from deeper tissues. In particular, a variety of metallic nanomaterials such as Pt nanoparticles[49], Pd nanoparticles[50], and gold nanorods (GNRs)[51] have been used as exogenous PA contrast agents because they strongly absorb NIR light and convert it into acoustic signals. In our study, we chose to use palladium (Pd) nanoparticles as the PA contrast component. Pd nanoparticles are attractive due to their lower cost compared to gold and their high structural stability under laser irradiation, ensuring a consistent PA signal over time.

1.6. Design Strategy for Dual-Modal CT/PA Imaging Agents

In developing a single contrast agent that can serve both CT and PA modalities, we carefully considered the requirements for each imaging technique and selected components that fulfill both sets of criteria: (1) CT imaging requirements: A good CT

doi:10.6342/NTU202501342

contrast agent should contain high-Z elements to effectively absorb X-rays, have good colloidal stability in biological fluids, and be small enough to accumulate in tumor tissue. We addressed these needs by choosing the Hf-EDB MOF as the base material. Hafnium's high atomic number provides strong X-ray attenuation, and the MOF's stable, porous structure ensures it remains well-dispersed and can be delivered to the tumor site. (2) PA imaging requirements: An effective PA contrast agent must have a strong absorption in the NIR region, high photothermal conversion efficiency to generate a robust ultrasound signal from light, and a stable PA signal under repeated laser pulses. We fulfilled these criteria by incorporating palladium nanoparticles, as Pd has broad NIR optical absorption and can withstand prolonged laser exposure without significant degradation.

To create a dual-modal agent, we loaded Pd nanoparticles into the pores of Hf-EDB. The resulting composite, termed Pd@Hf-EDB, integrates the X-ray contrast capability of Hf for CT with the NIR optical absorption of Pd for PA. In this single nanocomposite, the Hf-based MOF and the Pd nanoparticles work in tandem to provide contrast for both imaging modalities. This integration means that a single injected agent can be used to acquire both CT and PA images of a tumor.

doi:10.6342/NTU202501342

The combined CT/PA contrast agent provides complementary diagnostic information while potentially reducing the total amount of contrast material needed since one agent doubles for two modalities. The use of dual-modal agent instead of separate agents for CT and PA can simplify the imaging procedure and minimize patient exposure to foreign substances.

Moreover, the MOF structure of the agent offers large surface area and functional groups that could be further modified for specialized purposes, for example, attaching targeting ligands for targeting delivery, loading therapeutic drugs, or other theranostic applications

1.7. Research Objective

In summary, the objective of this study is to develop a dual-modal contrast agent by integrating Pd nanoparticles into Hf-MOF. This nanocomposite, Pd@Hf-EDB, is designed to enable both CT and PA imaging. The CT imaging performance will be evaluated in comparison with the clinically used iodine-based contrast agent iohexol, while the PA imaging performance will be compared with GNRs, a widely studied PA contrast agent.

doi:10.6342/NTU202501342

2. Experimental section

2.1. Materials

Ammonium chloride (NH_4Cl, >99.5%), copper iodide (CuI, >98%), iohexol (>98.0%), methyl 4-iodobenzoate (>98%), sodium chloride (NaCl, >99.5%), and trifluoroacetic acid were purchased from Tokyo Chemical Industry Co., Ltd. (Tokyo, Japan). Bis(triphenylphosphine)palladium(II) dichloride ($Pd(PPh_3)_2Cl_2$), Chloroform-d (99.8 atom%D), dichloromethane (DCM, 99%), dimethyl sulfoxide (DMSO), dimethyl sulfoxide-d_6 (99.8 atom%D), gold(III) chloride trihydrate (>99.9%), gold standard for ICP (999 ± 2 mg/l), hafnium standard for ICP (999 ± 3 mg/l), hafnium chloride ($HfCl_4$, 98%), HEPES solution (1M), hexadecyltrimethylammonium bromide (CTAB, >98%), palladium standard for ICP (999 ± 2 mg/l), potassium hydroxide (KOH), resazurin sodium salt, RPMI-1640 medium with L-glutamine, silver nitrate ($AgNO_3$, >99%), sodium borohydride ($NaBH_4$, >98%), sodium phosphate (Na_3PO_4, >96%), sodium bicarbonate ($NaHCO_3$), sodium phosphate monobasic (NaH_2PO_4, >99%) and triethylamine (TEA, >99%) were purchased from Sigma-Aldrich (St. Louis, MO). Potassium tetrachloropalladate(II) (K_2PdCl_4, 98%) was purchased from Acros Organics (Geel, Belgium). N,N-dimethylformamide (DMF), tetrahydrofuran (THF, >99.9%) were purchased from DUKSAN (Ansan-si, Korea). Toluene (>99.5%) was purchased from Echo Chemical Co., Ltd. (Miaoli, Taiwan). Ethanol (EtOH, >99.8%), hydrochloric acid

doi:10.6342/NTU202501342

(HCl, ≥ 37%) and nitric acid (HNO_3, ≥ 65%) were purchased from Honeywell (Charlotte, NC). 4-Ethynylbenzoic acid methyl ester (>97%) was purchased from Nova Materials Co., Ltd. (Taipei, Taiwan). Acetone (>99%), and hexane (>98.5%) were purchased from Union Chemical Works Ltd (Hsinchu, Taiwan). Ascorbic acid was purchased from Kanto Chemical Co., Inc (Tokyo, Japan). Agarose was from Bio-helix Co., Ltd. (New Taipei City, Taiwan). Antibiotic-antimycotic (Anti-anti) solution, fetal bovine serum (FBS), geltrex™, and trypsin-EDTA (10X) were from Gibco (Grand Island, NY). Mitotracker Green FM was from MedChemExpress (Monmouth Junction, NJ). Hoechst 33342 and LysoTracker™ deep red were purchased from Invitrogen (Carlsbad, CA). Quantifoil R2/2 circular holes on Au G200F1 finder grids (gold grids) was from Quantifoil Micro Tools GmbH (Großlöbichau, Germany).

Table 2.1. Materials

Chemical	Formula	Information
Ammonium chloride	NH_4Cl	>99.5%, Tokyo Chemical Industry Co., Ltd. (Tokyo, Japan)
Copper iodide	CuI	>98%, Tokyo Chemical Industry Co., Ltd. (Tokyo, Japan)
Iohexol	N/A	>98.0%, Tokyo Chemical Industry Co., Ltd. (Tokyo, Japan)

doi:10.6342/NTU202501342

Methyl 4-iodobenzoate	N/A	>98%, Tokyo Chemical Industry Co., Ltd. (Tokyo, Japan)
Sodium chloride	NaCl	>99.5%, Tokyo Chemical Industry Co., Ltd. (Tokyo, Japan)
Trifluoroacetic acid	N/A	Tokyo Chemical Industry Co., Ltd. (Tokyo, Japan)
Bis(triphenylphosphine) palladium(II) dichloride	$Pd(PPh_3)_2Cl_2$	Sigma-Aldrich (St. Louis, MO)
Chloroform-d	N/A	99.8 atom%D, Sigma-Aldrich (St. Louis, MO)
Dichloromethane	DCM	99%, Sigma-Aldrich (St. Louis, MO)
Dimethyl sulfoxide	DMSO	Sigma-Aldrich (St. Louis, MO)
Dimethyl sulfoxide-d6	N/A	99.8 atom%D, Sigma-Aldrich (St. Louis, MO)
Gold(III) chloride trihydrate	N/A	>99.9%, Sigma-Aldrich (St. Louis, MO)
Gold standard for ICP	N/A	999 ± 2 mg/l, Sigma-Aldrich (St. Louis, MO)
Hafnium standard for ICP	N/A	999 ± 3 mg/l, Sigma-Aldrich (St. Louis, MO)
Hafnium chloride	$HfCl_4$	98%, Sigma-Aldrich (St. Louis, MO)
HEPES solution	N/A	1M, Sigma-Aldrich (St. Louis, MO)

doi:10.6342/NTU202501342

Hexadecyltrimethylammonium bromide	CTAB	>98%, Sigma-Aldrich (St. Louis, MO)
Palladium standard for ICP	N/A	999 ± 2 mg/l, Sigma-Aldrich (St. Louis, MO)
Potassium hydroxide	KOH	Sigma-Aldrich (St. Louis, MO)
Resazurin sodium salt	N/A	Sigma-Aldrich (St. Louis, MO)
RPMI-1640 medium with L-glutamine	N/A	Sigma-Aldrich (St. Louis, MO)
Silver nitrate	$AgNO_3$	>99%, Sigma-Aldrich (St. Louis, MO)
Sodium borohydride	$NaBH_4$	>98%, Sigma-Aldrich (St. Louis, MO)
Sodium phosphate	Na_3PO_4	>96%, Sigma-Aldrich (St. Louis, MO)
Sodium bicarbonate	$NaHCO_3$	Sigma-Aldrich (St. Louis, MO)
Sodium phosphate monobasic	NaH_2PO_4	>99%, Sigma-Aldrich (St. Louis, MO)
Triethylamine	TEA	>99%, Sigma-Aldrich (St. Louis, MO)
Potassium tetrachloropalladate(II)	K_2PdCl_4	98%, Acros Organics (Geel, Belgium)
N,N-dimethylformamide	DMF	DUKSAN (Ansan-si, Korea)

doi:10.6342/NTU202501342

Tetrahydrofuran	THF	>99.9%, DUKSAN (Ansan-si, Korea)
Toluene	N/A	>99.5%, Echo Chemical Co., Ltd. (Miaoli, Taiwan)
Ethanol	EtOH	>99.8%, Honeywell (Charlotte, NC)
Hydrochloric acid	HCl	≥37%, Honeywell (Charlotte, NC)
Nitric acid	HNO_3	≥65%, Honeywell (Charlotte, NC)
4-Ethynylbenzoic acid methyl ester	N/A	>97%, Nova Materials Co., Ltd. (Taipei, Taiwan)
Acetone	N/A	>99%, Union Chemical Works Ltd. (Hsinchu, Taiwan)
Hexane	N/A	>98.5%, Union Chemical Works Ltd. (Hsinchu, Taiwan)
Ascorbic acid	N/A	Kanto Chemical Co., Inc. (Tokyo, Japan)
Agarose	N/A	Bio-helix Co., Ltd. (New Taipei City, Taiwan)
Antibiotic-antimycotic solution	N/A	Gibco (Grand Island, NY)
Fetal bovine serum (FBS)	N/A	Gibco (Grand Island, NY)
GeltrexTM	N/A	Gibco (Grand Island, NY)
Trypsin-EDTA (10X)	N/A	Gibco (Grand Island, NY)

doi:10.6342/NTU202501342

Mitotracker Green FM	N/A	MedChemExpress (Monmouth Junction, NJ)
Hoechst 33342	N/A	Invitrogen (Carlsbad, CA)
LysoTrackerTM deep red	N/A	Invitrogen (Carlsbad, CA)
Quantifoil R2/2 circular holes on Au G200F1 finder grids	N/A	Quantifoil Micro Tools GmbH (Großlöbichau, Germany)

2.2. Synthesis of 4,4'- (ethyne-1,2-diyl) dibenzoic acid (H_2EDB) Linker

The synthesis of H_2EDB can be divided into two parts, (1) the synthesis of precursor bis(4-(methoxycarbonyl)phenyl)acetylene (Me_2EDB) through Sonogashira cross-coupling reaction (Figure 2.1a) and (2) the subsequent hydrolysis and acidification of Me_2EDB to form 4,4'-(ethyne-1,2-diyl)dibenzoic acid (H_2EDB) (Figure 2.1b).[52]

doi:10.6342/NTU202501342

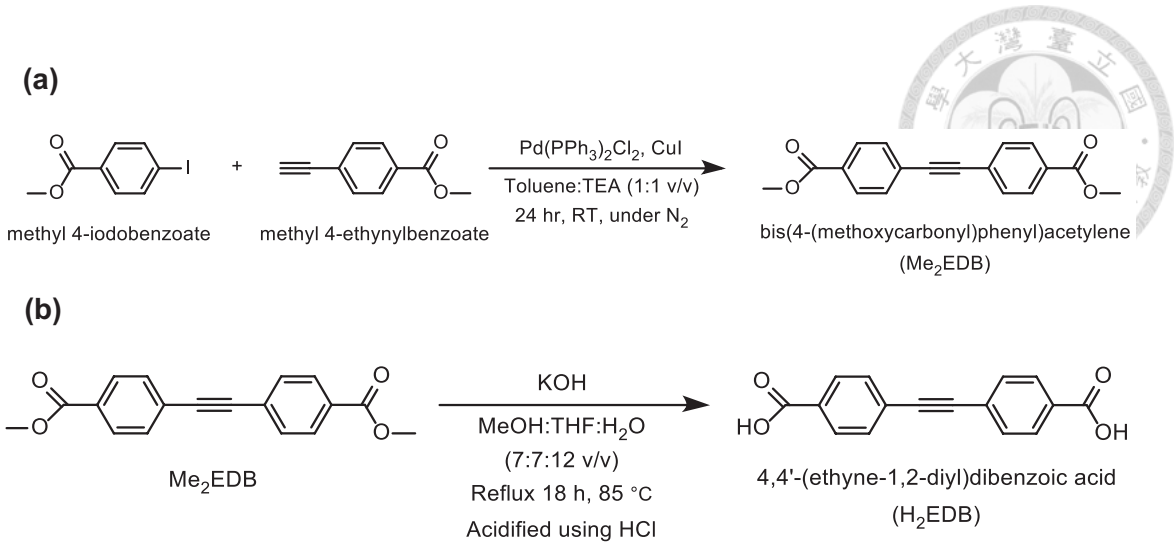

Figure 2.1. Synthesis of H_2EDB: (a) Preparing Me_2EDB through Sonogashira Cross-Coupling, (b) Hydrolysis of the Me_2EDB to form H_2EDB.

2.2.1 Synthesis of Me_2EDB

Methyl 4-iodobenzoate (2.62 g, 10.0 mmol) and methyl 4-ethynylbenzoate (1.602 g, 10.0 mmol) were added to a three-necked round bottom and dissolved in 50 mL of TEA/toluene mixture (v/v = 1:1) under magnetic stirring. The mixture was degassed in vacuum and stirred for 10 min before adding bis-triphenylphosphine-palladium (II) chloride ($PdCl_2(PPh_3)_2$) (176 mg, 0.25 mmol) and copper(I) iodide (10.0 mg, 0.05 mmol). Then, the mixture was stirred for 24 hours at room temperature under nitrogen flow. Next, the reaction mixture was filtered and washed sequentially with copious amounts of hexane, saturated NH_4Cl aqueous solution, saturated NaCl aqueous solution, and deionized (DI) water. The product was partially dried and redispersed in 30 mL of DCM.

doi:10.6342/NTU202501342

This mixture was stirred for at least two hours, collected by filtration, and dried overnight in a vacuum oven.

2.2.2 Synthesis of H_2EDB

Me_2EDB (0.639 g, 2.40 mmol) was suspended in 175 mL of a methanol/tetrahydrofuran mixture (v/v = 1:1). Then, 150 mL of DI water containing potassium hydroxide (1.346 g, 24.00 mmol) were added. The mixture was stirred and refluxed in a 75°C oil bath. The resulting solution was allowed to cool to a temperature below 40°C. And the product (i.e., H_2EDB) was precipitated by adding 10 mL of HCl to the mixture. The product was then collected via centrifugation following several rounds of sonication and washing to remove the residual HCl. Finally, the product was dried overnight in a vacuum oven for further characterizations including NMR analysiss.[41]

2.3. Synthesis of Hf-EDB

Hf-EDB was synthesized based on our previously reported protocol for achieving nanoscale Hf-PEB but modifying the linker accordingly.[53] Briefly, synthesizing Hf-EDB nanoparticles involves two steps: (1) Preparation of the Hf precursor and the H_2EDB solutions: Before synthesizing Hf-EDB, the stock solutions of $HfCl_4$ and H_2EDB were

doi:10.6342/NTU202501342

first prepared. The stock solution of $HfCl_4$ was prepared by adding $HfCl_4$ (2 mg/mL) to DMF and applying 30 min of sonication. The stock solution of H_2EDB was prepared by adding H_2EDB (2.5 mg/mL) to DMF and applying 10 min of sonication. To improve the dissolution of H_2EDB, the H_2EDB solution was heated for 20 min at 90°C using an oil bath. The resulting H_2EDB solution was cooled down and filtered with a 0.22 μm nylon syringe filter to remove the undissolved impurities. (2) Preparation of Hf-EDB nanoparticles using solvothermal reaction: To synthesize Hf-EDB, 50 mL of $HfCl_4$ stock solution and 100 μL of TFA were added to a 150 mL vial followed by the addition of 50 mL H_2EDB stock solution. The mixture was sonicated for 10 min and heated for 72 hours at 60°C using the program-controlled furnace. After the reaction, the product was cooled down, centrifuged, and washed once with 10 mL of DMF and 3 thrice with ethanol. Finally, the product was dried in a desiccator.

2.4. Incorporation of Pd NPs in Hf-EDB

The procedure was modified from our previous work.[41] Hf-EDB (61 mg) was added to 5.0 mL of H_2O and sonicated for 4 mins using a probe sonicator. Then, 2.5 mL of H_2O containing K_2PdCl_4 (42.75 mg) was added to the Hf-EDB suspension. The mixture was stirred for 30 min at room temperature. The resulting brownish particles (i.e., Pd^{2+}@Hf-EDB) were collected by centrifugation (15000 rpm, 15 min) and rinsed 2 times with 5

doi:10.6342/NTU202501342

mL of H_2O (each time the mixture was sonicated for 10 min). Then, the particles were re-suspended in 5.0 mL of H_2O, and 2.5 mL of ice-cold water containing $NaBH_4$ (49.55 mg) was added. The mixture was stirred for 30 min at room temperature. Finally, the blackish product was centrifuged, rinsed twice with 5 mL of H_2O and once with 5 mL of EtOH before drying in vacuum. The overall preparation procedure of Pd@Hf-EDB is summarized in Figure 2.2.

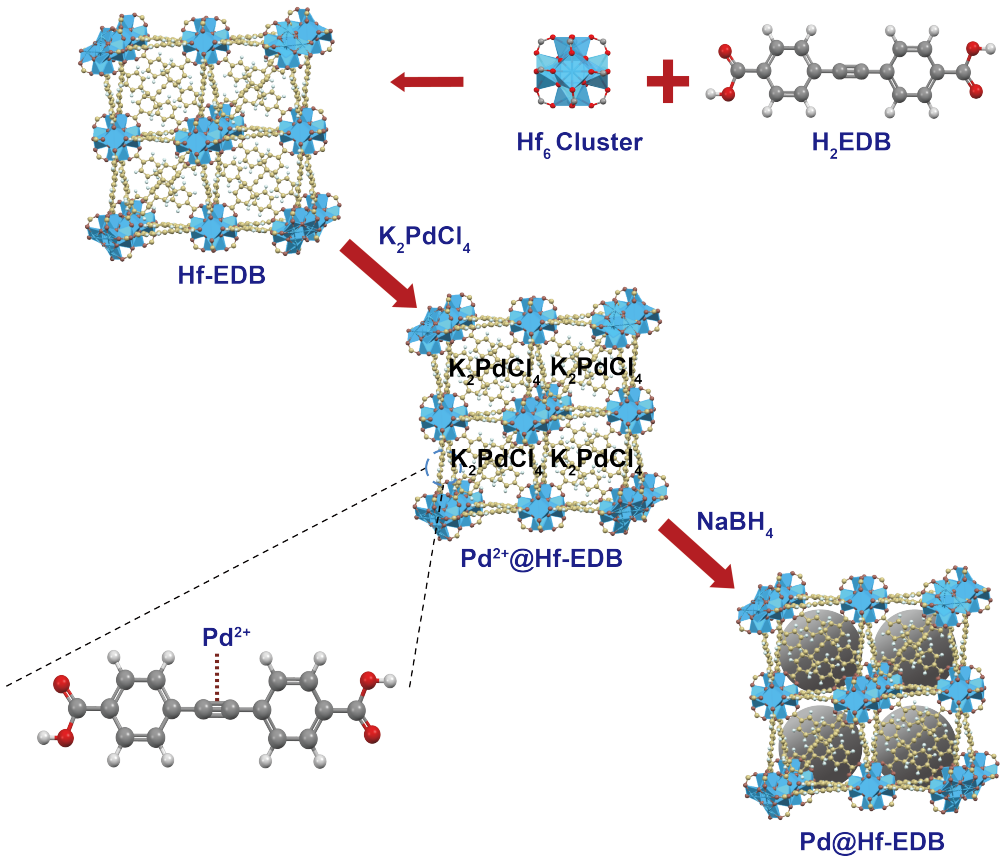

Figure 2.2. Synthesis of the Pd@Hf-EDB

doi:10.6342/NTU202501342

2.5. Synthesis of Gold Nanorods

The protocol of GNR is from our previous work.[54] The first step of preparing gold seed solution is as follows: 5 mL of 0.5 mM $HAuCl_4$ was mixed with 5 mL of 0.2 M CTAB solution, and 0.6 mL of fresh 0.01 M $NaBH_4$ was injected into the solution rapidly. The mixed solution was stirred for two hours, and the color of the mixed solution was changed from yellow to brownish-yellow. The second step was preparing the growth solution: 75 mL of 1 mM $HAuCl_4$ was mixed with 75 mL of 0.2 M CTAB solution and 3.75 mL of 4 mM $AgNO_3$ to control longitude absorption in the near-infrared region. 1.05 mL of 78mM ascorbic acid was added into the solution to reduce gold from Au^{3+} to Au^{1+}. The solution color turned from yellow to colorless in seconds. Next, 180 μL of seed solution was added and kept in a 37 °C water bath for 24 h. The resulting solution was centrifuged at 20000 rpm for 10 min and washed thrice with water.

2.6. Characterization

2.6.1 Scanning Electron Microscopy (SEM)

For Hf-EDB and Pd@Hf-EDB samples, the powders were dispersed in ethanol and dropped onto silicon wafers. The silicon wafers with the samples were fixed onto the sample stub using conductive carbon tape. The SEM images were then acquired with an

doi:10.6342/NTU202501342

acceleration voltage of 10 kV using a cold-field emission scanning electron microscope (Hitachi S-4800) from Hitachi (Tokyo, Japan)

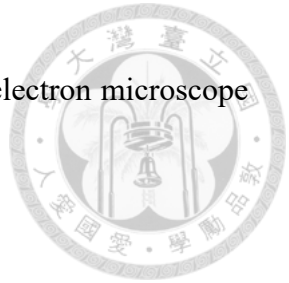

2.6.2 X-ray Diffraction (XRD)

X-ray diffraction patterns of the samples were measured using a Miniflex diffractometer from Rigaku (Tokyo, Japan), with Cu Kα radiation (λ = 1.5418 Å). Simulated patterns were generated using the crystallographic information files (CIF) of Hf-EDB retrieved from the CCDC 1062509 (https://www.ccdc.cam.ac.uk).[55, 56]

2.6.3 Zeta Potential

Hf-EDB (0.05 mg/mL) or Pd@Hf-EDB (0.05 mg/mL) were sonicated to disperse in a 10 mM phosphate buffer (6.5 mM NaH_2PO_4 + 3.5 mM Na_3PO_4, pH 7.32) and zeta potential was measured using a Zetasizer Nano instrument from Malvern Panalytical (Malvern, UK).

2.6.4 Particle Size

Hf-EDB or Pd@Hf-EDB disperse in ethanol or DI water via sonicated and measured using a Zetasizer Nano instrument from Malvern Panalytical (Malvern, UK).

doi:10.6342/NTU202501342

2.6.5 Specific Surface Area

The N_2 adsorption isotherms of Hf-EDB and Pd@Hf-EDB were measured with the ASAP 2020 N_2 adsorption instrument from Micromeritics Instrument Corporation (Norcross, USA). The specific surface areas of the materials were determined using the recently reported Brunauer-Emmett-Teller Surface Identification (BETSI) method, using the BETSI v2.0 software retrieved from GitHub (https://github.com/fairen-group/betsi-gui).

2.6.6 Nuclear Magnetic Resonance (NMR)

To characterize the structure of linkers, the samples' nuclear magnetic resonance (NMR) spectra were obtained using an AVIII 500 MHz NMR spectrometer from Bruker (Billerica, MA). The data analysis was conducted using Bruker TopSpin Software.

2.6.7 Transmission Electron Microscope (TEM)

The distribution of the Pd NPs in Hf-EDB and the energy dispersive spectroscopy (EDS) mapping were observed using a JEM-2100F field-emission transmission electron microscope (FE-TEM) from JEOL Ltd. (Akishima, Japan).

doi:10.6342/NTU202501342

2.6.8 Inductively coupled plasma optical emission spectrometer (ICP-OES)

The weight percent of Pd in Pd@Hf-EDB was obtained using an iCAP PRO inductively coupled plasma optical emission spectrometer (ICP-OES) from Thermo Fisher Scientific (Waltham, USA).

2.6.9 Ultraviolet-visible (UV-Vis)

Ultraviolet-visible (UV–Vis) spectra of the materials were obtained using a UV-Vis/NIR Spectrophotometer V-670 from JASCO (Tokyo, Japan).

2.7. Cell Line

The human pancreatic cancer cell line BxPC-3 was obtained from the National Health Research Institute (NHRI) in Miaoli, Taiwan. The cells were grown in RPMI 1640 medium with L-glutamine supplemented with 1.5 g/L sodium bicarbonate, 10 mM HEPES, 10% FBS, and 1% anti-anti in a humidified atmosphere of 5% CO^2 at 37 ℃.

2.8. Cell Subculture

When the cells reached 80% confluence in the cell culture dish 100x20 well plate,

doi:10.6342/NTU202501342

the supernatant was removed, and the cells were rinsed with PBS. Then, 1 mL of trypsin was added, and the plate was placed in the incubator for 5 minutes. The cells were dispersed in 5 mL of complete RPMI medium and centrifuged at 1000 rpm for 5 minutes. They were then sub-cultured at a 1:3 ratio, adding 10 mL of complete medium before returning to the incubator.

2.9. Cell Viability

The cytotoxicity of materials was determined with the AlamarBlue™ assay (Figure 2.3). Typically, 2×10^4 of BxPC-3 or RAW 264.7 cells in 100 μL of complete RPMI or DMEM medium was added to a well of a 96-well culture plate and incubated in a 37°C, 5% CO_2 incubator. The culture medium was replaced on the second day with 100 μL of complete RPMI or DMEM medium containing Hf-EDB and Pd@Hf-EDB (0-250 μg/mL). The cells were incubated for 24 hours. And 20 μL of phosphate buffered saline (PBS) containing resazurin sodium salt (0.15 mg/mL) was added to the well. After two hours of incubation, the fluorescence intensities (FI, $\lambda_{Ex}/\lambda_{Em}$ = 560/590 nm) of the samples were measured using an SpectraMax iD3 Multi-Mode Detection Platform (Molecluar Devices), and the background readings were subtracted using the wells containing culture medium, nano-material, and AlamarBlue reagent but without cells (Figure 2.4). The relative viabilities of the cells were then calculated using the equation: relative viability (%) =

doi:10.6342/NTU202501342

FI_{Sample} / $FI_{Control}$ × 100, where FI_{Sample} is the FI of the sample, and $FI_{Control}$ is the mean FI of the control (0 μg/mL) group.

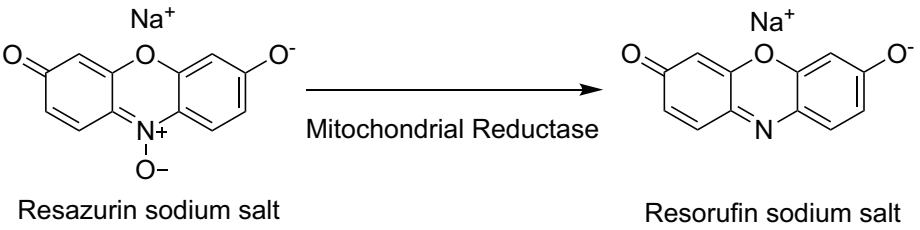

Figure 2.3 Mechanism of the AlamarBlue assay

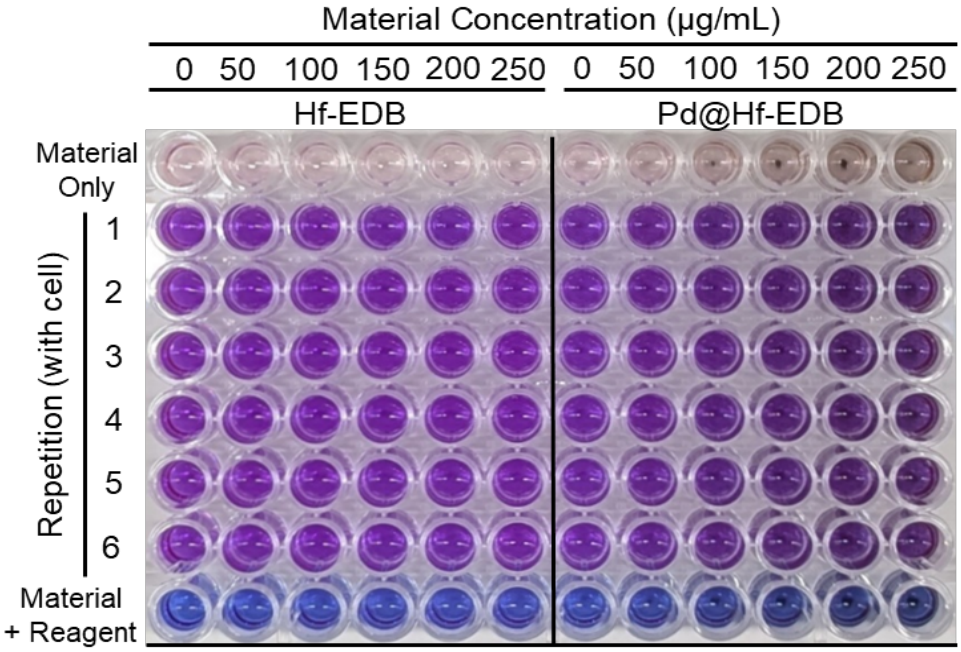

Figure 2.4. The detail of the AlamarBlue assay experiment

2.10. Observing the Cellular Uptake of Pd@Hf-EDB using SXT.

BxPC-3 cells were cultured on carbon-coated gold grids for SXT experiments. To improve the cell adhesion, the carbon-coated sides of gold grids were glow-discharged

doi:10.6342/NTU202501342

(15 mA, 25 seconds) using a PELCO easiGlow™ system from Ted Pella, Inc. (Redding, CA) to induce hydrophilicity. Subsequently, the prepared gold grids were positioned within a customized PDMS well. Then, 170 μL of BxPC-3 cell suspension (1×10^5 cells/mL in complete RPMI) was added to each PDMS well. The cells were cultured overnight in a 37°C, 5% CO_2 incubator. For the group treated with Pd@Hf-EDB, the culture medium was replaced with 170 μL of complete RPMI containing 100 μg/mL of Pd@Hf-EDB. The cells were then cultured for an additional eight hours in the same incubator. Following the incubation period, the cells were rinsed two times with PBS and stained with a staining solution containing Hoechst 33342 (4 μg/mL), Mitotracker Green FM (1μM), and lysotracker Deep Red solution (1 μM) in serum-free RPMI medium at room temperature. The gold grid was rinsed with PBS, and then a 100 nm gold colloid solution (BBI Solutions, Crumlin, UK) was added as fiducial markers before the grid was plunged into liquid ethane using an EM GP plunge freezer from Leica (Vienna, Austria). The sample was kept in liquid nitrogen, and the locations of the cells on the grid were searched using Axio Imager A2 wide-field fluorescence microscopy from Zeiss. The fluorescence microscopy images of nuclei (Hoechst 33342), mitochondria (Mitotracker Green FM), and acidic compartments (lysotracker Deep Red) within the cells were also captured. After the screening, SXT was performed at the Taiwan Photon Source (TPS) 24A1 beamline at the National Synchrotron Radiation Research Center (NSRRC,

doi:10.6342/NTU202501342

Hsinchu, Taiwan)[57]. Flat-field correction of the SXT images was performed using customized software, and the 3D reconstruction of the tomogram was performed using IMOD software (https://bio3d.colorado.edu/imod/). The cryo-fluorescence and X-ray microscopy images (using the tilt series image at 0°) were correlated using Fiji software and Inkscape software (https://inkscape.org/). The channels were aligned according to the nucleus.

2.11. In vitro CT imaging

For in vitro CT imaging, agarose powder was dissolved in DI water at 65 °C to obtain a 2% (w/v) agarose solution. Separately, imaging materials (Hf-EDB, iohexol, and Pd@Hf-EDB) were individually dispersed in DI water at 40 mg/mL using a probe sonicator (Q700, Qsonica LLC, Newtown, CT, USA) equipped with a probe (CL-334) at an intensity setting of 10 for 4 min. Subsequently, equal volumes of the heated 2% agarose solution and each sonicated dispersion were thoroughly mixed to yield stock solutions containing 1% agarose and 20 mg/mL of the imaging materials. Further serial dilutions were performed by mixing these stock solutions with a 1% agarose solution, achieving final material concentrations of 10, 5, and 2.5 mg/mL. Aliquots of 100 μL from each diluted concentration were then transferred into 1.5 mL Eppendorf tubes and stored in a refrigerator prior to CT imaging analysis. CT scanning was conducted using a

doi:10.6342/NTU202501342

PET/SPECT/CT Tri-Modality Imaging System (GAMMA MEDICA-IDEAS, FLEX Triumph) with an X-ray tube voltage of 50 kVp. We first scanned the background, defining the grayscale value of air as -1000 and 2% agarose as 0. Subsequently, we scanned samples at different concentrations. Using Dragonfly software, we integrated the grayscale values of the samples and calculated the average. This mean gray value (MGV) was then used in the formula $HU = 1000 \times (MGV_{sample} - MGV_{agarose}) / (MGV_{agarose} - MGV_{air})$ to determine the HU values corresponding to each concentration. The relationship between HU values and concentration was linear as the concentration increased.

2.12. In vitro PA imaging

For in vitro PA imaging, we dispersed Pd@Hf-EDB and GNRs in water. Pd@Hf-EDB was prepared at concentrations of 200, 100, 50, and 25 ppm, each with a volume of 20 mL. GNRs were prepared based on the peak OD values, with OD = 1, 0.5, 0.25, 0.125, and 0.0625 in 20 mL volumes. The samples were then placed in 100 × 20 mm cell culture dishes. PA scanning was conducted using a PAI system (FUJIFILM VisualSonics Inc. Vevo LAZR system). We applied a gel to the concave part of the PA ultrasound probe to serve as a medium for sound transmission, preventing noise from air interference. The probe was then placed on the surface of the samples, and scanning was performed at

doi:10.6342/NTU202501342

wavelengths ranging from 680 to 950 nm, with scanning resolution of 10 nm. Using Vevo LAB software, we averaged five PA measurements at each wavelength and plotted these averages against the corresponding concentrations.

To simulate the vascular environment, the Pd@Hf-EDB and GNRs were dispersed in solutions at a concentration of 100 ppm, and each mixture was then injected into polyethylene tubing with an inner diameter of 0.38 mm using insulin syringes. The concentration of GNRs was determined using ICP-OES. And, PA scanning was conducted at 750, 800, 850, 900, 950, and 975 nm using a custom-made Dual-mode US/PA imaging system from the NHRI Liao lab. The integral of images values of PA signals were extracted using MATLAB to represent the characteristic PA signals for each condition.

2.13. Animal Model

All animal experiments were carried out according to guidelines accepted by the National Health Research Institutes Laboratory Animal Center. This animal model study involves four male CAnN.Cg-Foxn1nu/CrlNarl mice, approximately 7 weeks old, were born on October 7, 2024, and received from the National Laboratory Animal Center

doi:10.6342/NTU202501342

(NLAC) in Tainan, Taiwan, on November 15, 2024. The experiment was conducted on November 27, 2024 with an assigned protocol number of NHRI-IACUC-113079-M1. Briefly, to establish the xenograft tumor model, 10^6 BxPC-3 cells were suspended in 50 μL of serum-free medium and mixed with 25 μL of Geltrex, then injected subcutaneously into the right thigh of the mice using a 0.5 mL 28G insulin syringe from BD Medical – Diabetes Care. The body weight of the mice ranged from 19 to 24 grams. Xenografted tumor size was measured weekly in 2 orthogonal directions using calipers, and the tumor volume (mm^3) was estimated using the equation: length × $(width)^2$ × 0.5. The mice were sacrificed at 7 weeks after administration of the contrast agents.[58]

doi:10.6342/NTU202501342

3. Results and Discussion

3.1. Synthesis and Characterization of H_2EDB Linker

The H_2EDB was synthesized using Sonogashira Cross-Coupling with methyl 4-iodobenzoate and methyl 4-ethynylbenzoate. Sonogashira Cross-Coupling forms carbon-carbon bonds between an alkyne and an aryl or vinyl halide. It typically involves the use of a palladium catalyst and a copper co-catalyst. An amine base environment deprotonates the alkyne, making it more nucleophilic. We synthesized the linker ourselves considering commercial H_2EDB linkers are challenging to acquire and often contain impurities. Our process for Me_2EDB utilized nitrogen gas to reduce side reactions, while dichloromethane was employed to remove colored impurities. The NMR spectrum of Me_2EDB in Figure 3.1a showed that the peak areas in $CDCl_3$ matched the expected hydrogen ratios, indicating successful synthesis of Me_2EDB. Additionally, the absence of any unidentified peak except minor peaks from residual solvent at 7.26 ppm and water at 1.56 ppm in $CDCl_3$ solvent indicated that the Me_2EDB is of relatively high purity. Next, Me_2EDB was hydrolyzed to H_2EDB salts with KOH and converted to H_2EDB using HCl. The NMR spectrum of H_2EDB in Figure 3.1b showed that the peak areas matched the expected hydrogen ratios, and H_2EDB is relatively pure, with only minor peaks from residual solvent at 2.5 ppm and water at 3.33 ppm in DMSO-d_6 solvent. The carboxyl peak in the NMR spectrum was usually weak and broad because the proton is involved in the rapid

doi:10.6342/NTU202501342

proton-exchange effect. This exchange occurs with the solvent or other carboxyl groups, causing the signal to become averaged and more diffuse. Therefore, we also showed the ^{13}C spectrum of the H_2EDB in Figure 3.2, which matched the structure of H_2EDB without an unidentified peak. Overall, NMR results confirmed that H_2EDB linkers have been successfully synthesized.

doi:10.6342/NTU202501342

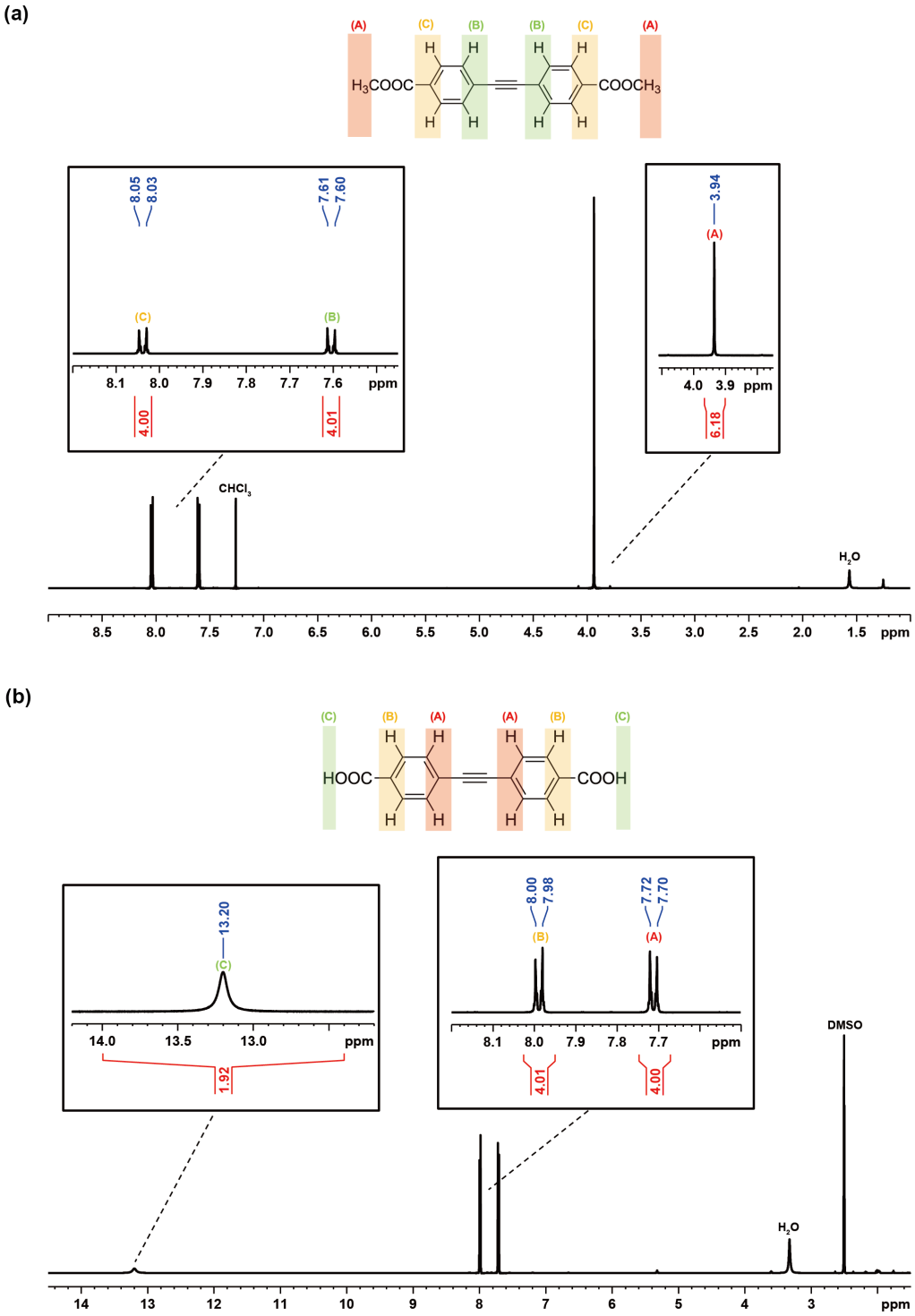

Figure 3.1. Nuclear magnetic resonance (NMR) spectra. (a) NMR ^{1}H spectrum of Me_2EDB, with $CDCl_3$ as the solvent, (b) NMR ^{1}H spectrum of H_2EDB, with DMSO-d_6 used as the solvent.

doi:10.6342/NTU202501342

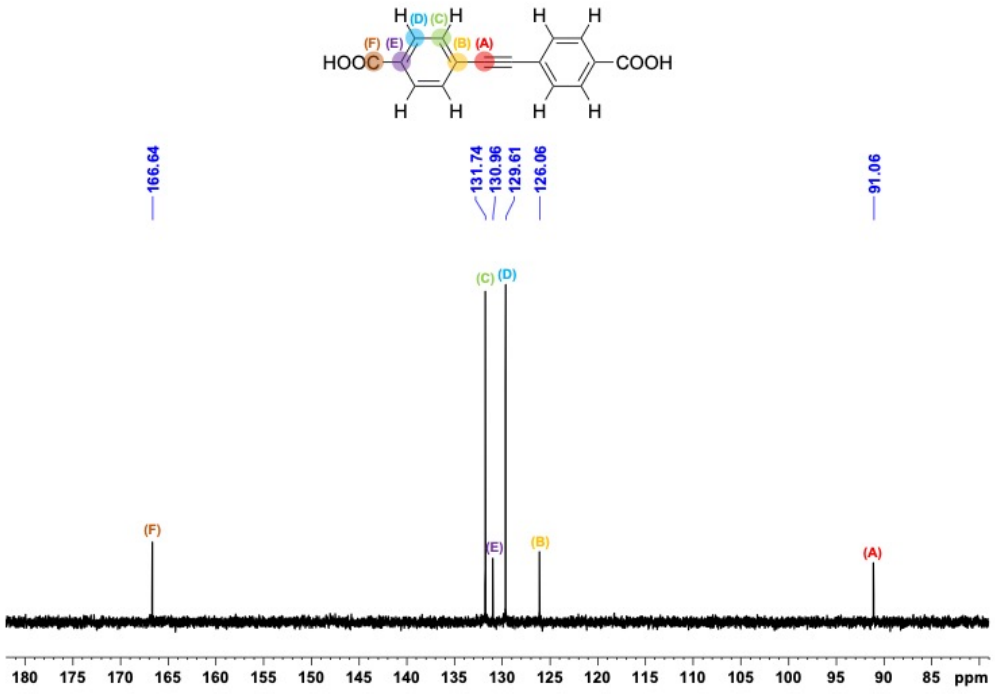

Figure 3.2. The NMR ^{13}C spectrum of the H_2EDB, with DMSO-d_6 used as the solvent.

3.2. Synthesis and Characterization of Hf-EDB nanoparticles

Previously, we had reported that nanoscale Hf-PEB can be synthesized by utilizing trifluoroacetic acid as the modulator through the solvothermal method.[59] In this work, we changed the linker from H_2PEB to H_2EDB and used a similar ratio of the reactants to form a UiO type Hf-EDB $[Hf_6O_4(OH)_4(EDB)_6]_n$ MOFs.

doi:10.6342/NTU202501342

The X-ray diffraction (XRD) pattern of as-synthesized Hf-EDB is shown in Figure 3.3a, which was in agreement with that of the simulated structure of Hf-EDB.[60] The five sharp characteristic peaks of Hf-EDB corresponding lattice planes (1 1 1), (2 0 0), (2 2 0), (3 1 1), and (2 2 2) was identified, which indicated high crystallinity and the absence of unidentified peaks concluded the purity of the as-synthesized MOF.

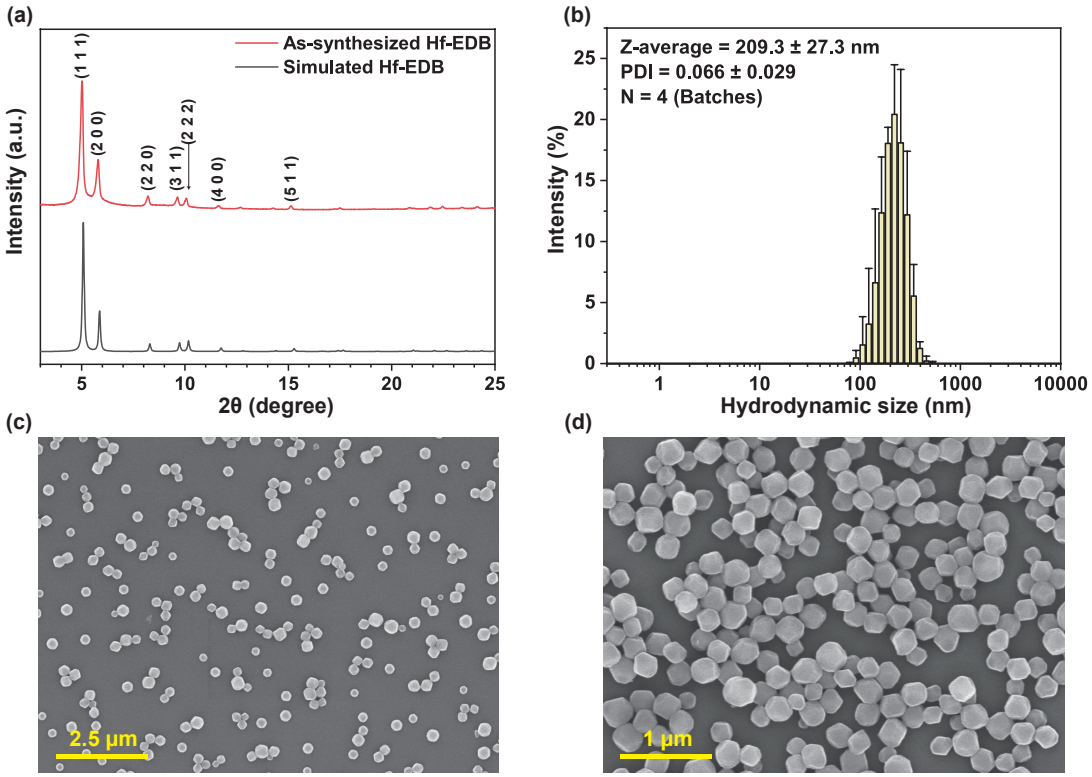

Figure 3.3. Characterization of Hf-EDB nanoparticles. (a) XRD patterns of Hf-EDB, (b) Size distribution of Hf-EDB obtained from DLS measurements with four batches (n = 4), (c) SEM image of Hf-EDB with low magnification, (d) SEM image of Hf-EDB with high magnification.

doi:10.6342/NTU202501342

Particle size and dispersity of nanoparticles are critical factors in biomedical applications. Nanoparticles with a size of approximately 200 nm are more easily engulfed by cells.[61] Therefore, during the synthesis of Hf-EDB nanoparticles, we utilized TFA as a modulator to regulate the particle size. We employed DLS analysis to uncover particle size and dispersibility information. Showed in Figure 3.3b and Table 2.1, the size distribution of Hf-EDB had a Z-average of 209.3 ± 27.3 nm (n = 4) and a PDI of 0.066 ± 0.029 (n = 4). In the previous sentence, (n=4) refers to four batches of Hf-EDB synthesized at different times. The small PDI indicated good dispersity, and the particle size of approximately 200 nm aligns well with our requirements in biomedical applications. We also measured the zeta potential of Hf-EDB to obtain more information about the dispersibility. The results showed a zeta potential of approximately -37.9 ± 6.38 mV in PB buffer (pH 7.3), which indicated good dispersibility in a physiological environment (Table 3.1). We also measured the elemental composition of Hf-EDB using ICP-OES, and the results showed that Hf accounted for 37.60 ± 2.23 %, similar to the molecular weight percent of Hf in Hf-EDB.

doi:10.6342/NTU202501342

Table 3.1. Hydrodynamic Size and PDI of Hf-EDB and Pd@Hf-EDB

Materials	Hydrodynamic size (nm)	PDI
Hf-EDB	209.3 ± 27.3	0.066 ± 0.029
Pd@Hf-EDB	265.1 ± 18.2	0.018 ± 0.038

From the SEM images, we could observe that Hf-EDB aggregation is insignificant in the low-magnification image (Figure 3.3c). In the high-magnification image (Figure 3.3d), Hf-EDB nanoparticles exhibit transparent particle outlines and a uniform size of approximately 200 nm, consistent with the results obtained from DLS measurements.

3.3. Incorporation of Pd NPs and Characterization of Pd@Hf-EDB nanoparticles.

The ethynyl groups on the H_2EDB linkers possess unique π-donor and π-acceptor properties that allow for strong interactions with noble metal ions. The ethynyl groups within Hf-EDB first absorbed the Pd^{2+} ions through stirring. Next, we used $NaBH_4$ to reduce Pd^{2+} ions into Pd nanoparticles called Pd@Hf-EDB.

doi:10.6342/NTU202501342

The SEM image of Pd@Hf-EDB nanoparticles (Figure 3.4a), showed transparent particle outlines with some protrusions on the surface and a uniform size of approximately 200 nm. Further analysis using DLS was conducted to shed light on the observed particle size and dispersibility. Showed in Figure 3.4b, the size distribution of Pd@Hf-EDB had a Z-average of 265.1 ± 18.2 nm (n = 4) and a PDI of 0.183 ± 0.038 (n = 4). The results indicate that the Z-average and PDI of Pd@Hf-EDB are larger than Hf-EDB's. This can be attributed to the fact that the synthesis of Pd@Hf-EDB is based on pre-synthesized Hf-EDB, meaning the state of Hf-EDB influences its characteristics. The presence of significant signals at the large particle size intensities in the size distribution due aggregation and the introduction of Pd are inherently expected to bring about a slight increase in the Z-average. Despite these factors, the particle size and dispersibility of Pd@Hf-EDB are still suitable for biomedical applications. Additionally, the observed zeta potential of approximately -39.6 ± 7.58 mV in PB buffer (pH 7.3), indicated good dispersibility in a physiological environment. We also measured the elemental composition of Pd@Hf-EDB using ICP-OES, and the results showed that Pd accounted for 25.74 ± 1.24 % (Table 3.2).

doi:10.6342/NTU202501342

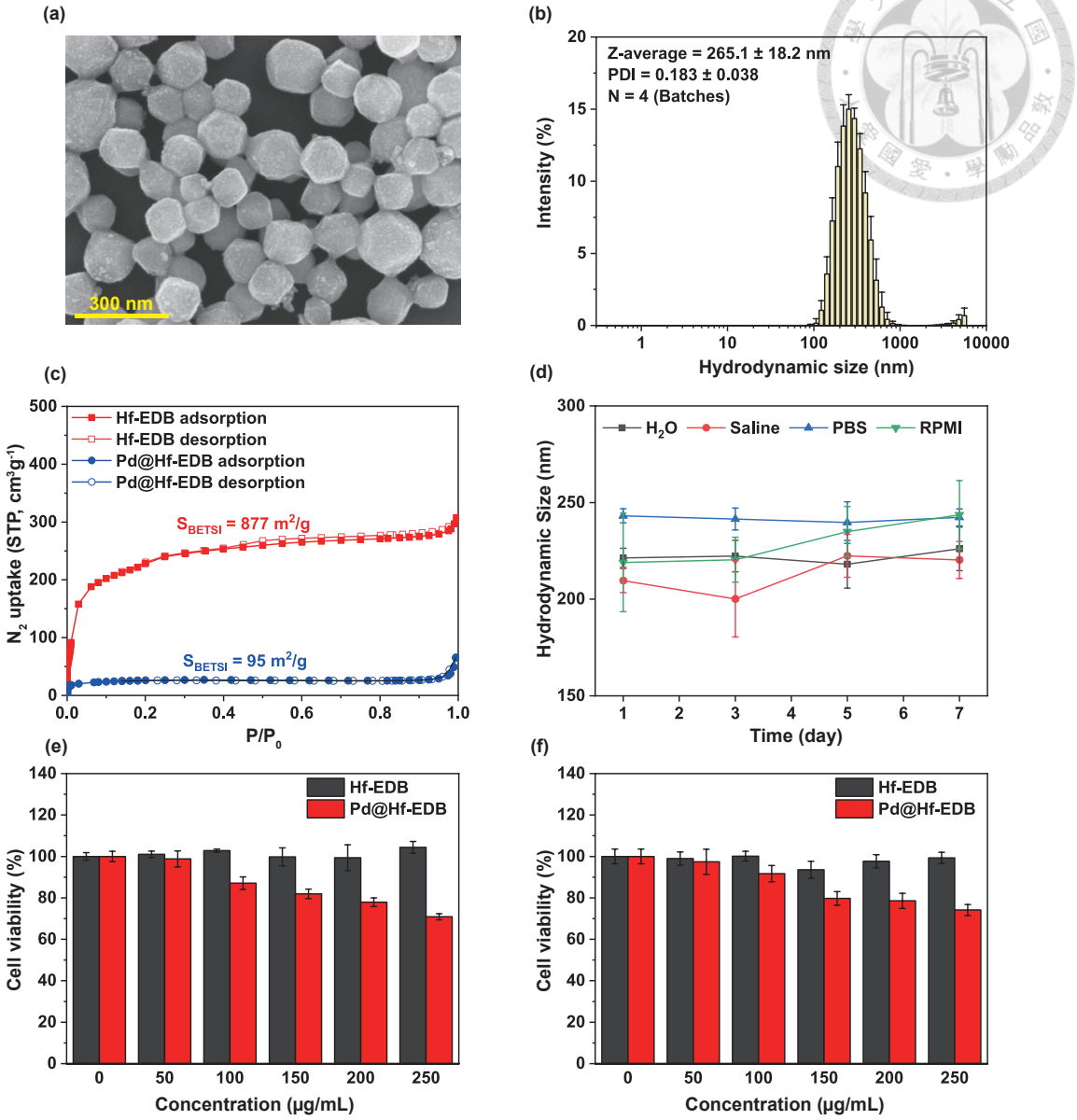

Figure 3.4. Characterization of Pd@Hf-EDB nanoparticles. (a) SEM image of Pd@Hf-EDB, (b) Size distribution of Pd@Hf-EDB obtained from DLS measurements with four batches (n = 4), (c) N_2 adsorption and desorption isotherms of Hf-EDB and Pd@Hf-EDB, (d) Hydrodynamic size of Pd@Hf-EDB dispersed in different media at different storage time, (e) Cell viability of BxPC-3 cells treated with Hf-EDB and Pd@Hf-EDB, (f) Cell viability of RAW 264.7 cells treated with Hf-EDB and Pd@Hf-EDB.

doi:10.6342/NTU202501342

Table 3.2. Metal weight percent and ζ-potential of Hf-EDB and Pd@Hf-EDB

Materials	Metal wt%	ζ-potential (mV)
Hf-EDB	Hf: 37.60 ± 2.23	-37.9 ± 6.38
Pd@Hf-EDB	Pd: 25.74 ± 1.24	-39.6 ± 7.58

To demonstrate the long-term stability of the Pd@Hf-EDB as a contrast agent, we measured its hydrodynamic size using DLS over a period of 7 days (Figure 3.4d). The measurements were conducted in H_2O, normal saline, PBS, and RPMI medium. The results clearly show that the contrast agent does not exhibit any significant changes in hydrodynamic size across these media for at least 7 days, indicating excellent stability. Additionally, to further assess the stability of Hf and Pd elements within the contrast agent, we monitored their leakage using ICP-OES analysis (Figure 3.5). Notably, after storage for 7 days, the released Pd was less than 0.5%, while Hf was nearly undetectable, demonstrating the contrast agent's good chemical stability.

doi:10.6342/NTU202501342

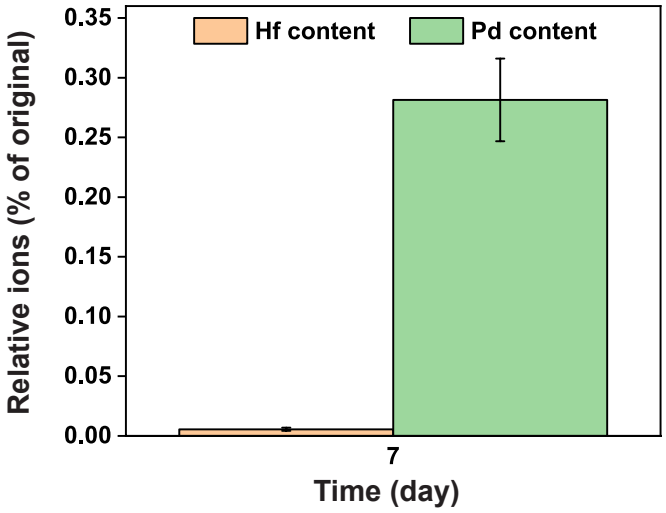

Figure 3.5. Percentage of original Hf and Pd content remaining in the supernatants of Pd@Hf-EDB (1 mg/mL) after being stored at 37 °C for 7 days.

We also used nitrogen adsorption-desorption isotherms to observe the changes in specific surface area before and after loading Pd nanoparticles into Hf-EDB (Figure 3.4c). The results showed that the specific surface area decreased from 877 m^2/g for Hf-EDB to 95 m^2/g for Pd@Hf-EDB. This indicated that the successful loading of Pd caused a reduction in specific surface area due to the filling of pores.

High-resolution transmission electron microscopy (HR-TEM) was performed to examine the morphology of the Pd@Hf-EDB. The HR-TEM images (Figure 3.6a) clearly

doi:10.6342/NTU202501342

showed the spherical Pd nanoparticles exhibiting distinct electron diffraction patterns. Furthermore, the HR-TEM in the inset in Figure 3.6a showed lattice fringes of 0.23 nm which can be attributed to the (1 1 1) plane of the Pd crystal (Figure 3.7). The EDS mapping images of Pd@Hf-EDB revealed that Hf and Pd were uniformly distributed throughout the particles (Figure 3.6b). Given that Hf signals are derived from Hf-EDB and Pd signals are derived from Pd nanoparticles, we concluded that Pd nanoparticles are successfully loaded into the pores of Hf-EDB.

doi:10.6342/NTU202501342

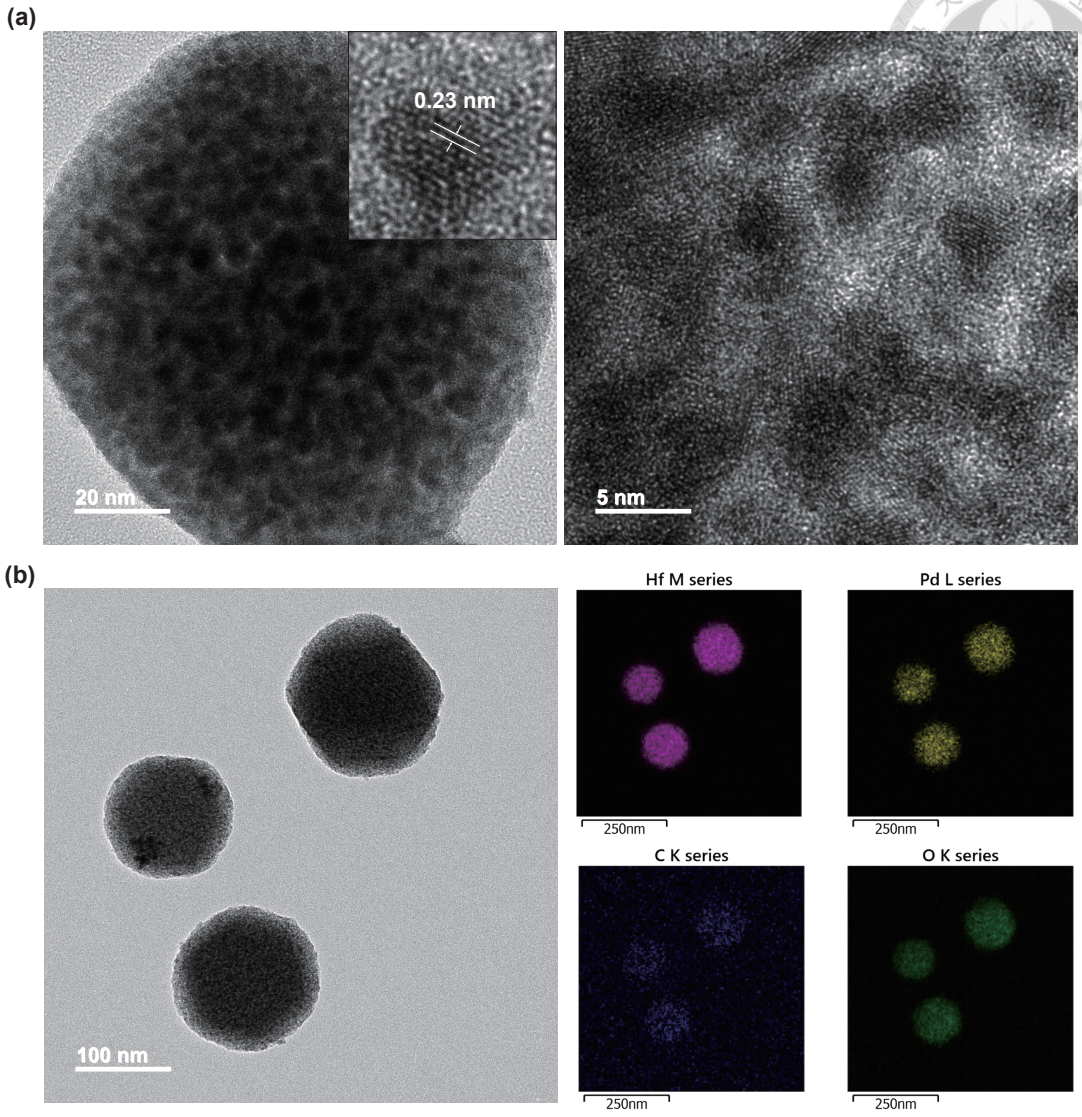

Figure 3.6. (a) HR-TEM image of Pd@Hf-EDB, (b)EDS mapping results of Pd@Hf-EDB

doi:10.6342/NTU202501342

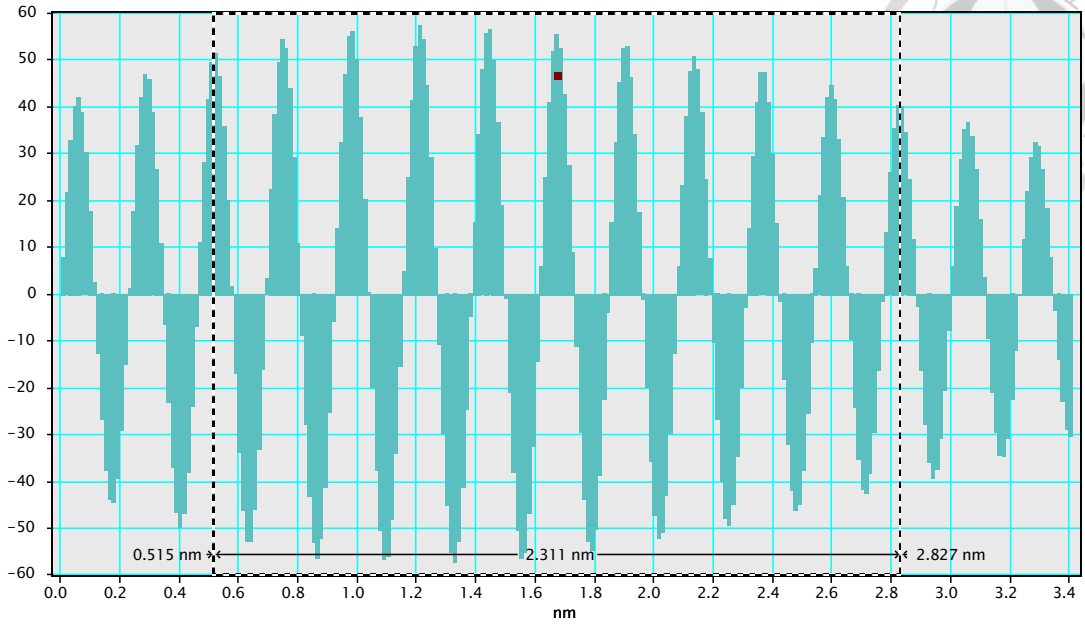

Figure 3.7. Lattice fringes of the Pd nanoparticles inside the Hf-EDB.

The optical properties of the Pd@Hf-EDB nanoparticles were assessed through UV-vis spectral analysis (Figure 3.8a). The UV-vis spectrum revealed enhanced absorption in the 350 to 1100 nm range, which is attributed to Pd nanoparticles' strong inter-band absorption. This characteristic makes them suitable as PAI contrast agents in near-infrared (NIR) regions.

doi:10.6342/NTU202501342

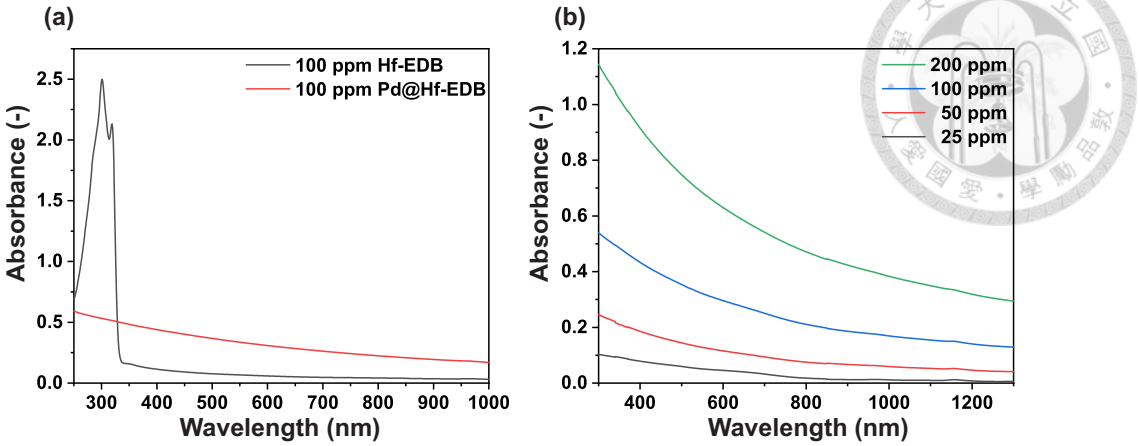

Figure 3.8. (a) The absorbance spectra of Hf-EDB and Pd@Hf-EDB. (b) The absorbance spectra of Pd@Hf-EDB dispersed in water at different concentrations.

3.4. Cell Viability

Before conducting *in vivo* experiments, we investigated the materials' toxicity to cells. As an imaging contrast agent for tumor cells, we want the materials to have no direct cytotoxicity to the tumor cells. Therefore, we used the AlamarBlue™ assay to measure the cytotoxicity of the materials on tumor cells. We selected the BxPC-3 and RAW 264.7 cell lines as our cell models and cultured the materials at 0, 50, 100, 150, 200, and 250 μg/mL with the cells. Each well in the 96-well plate contained approximately $2x10^4$ cells. The results (Figure 3.4e, f) showed that Hf-EDB did not significantly reduce cell viability within this concentration range in both cell lines, while Pd@Hf-EDB maintained 85% cell viability in BxPC-3 and 90% in RAW 264.7 at 100

doi:10.6342/NTU202501342

μg/mL. However, as the concentration continued to increase, there was a noticeable decline, with cell viability dropping to 70% in BxPC-3 and 75% in RAW 264.7 at 250 μg/mL. Therefore, we will use a 100 μg/mL concentration in subsequent imaging contrast agent efficacy experiments. Testing RAW 264.7 cells in addition to tumor cells is important to assess the cytotoxicity on macrophages, which can provide preliminary insights into the Pd@Hf-EDB's potential effects on the immune system.

3.5. Observing the Cellular Uptake of Pd@Hf-EDB using SXT

To observe the cellular uptake of materials, we chose the NSRRC TPS 24A beamline: soft x-ray tomography (SXT). Compared to typical X-ray tomography, this beamline offers higher resolution while enabling visualization of organelles inside the cells via SXT. Due to the lower energy of soft X-rays, the organelles maintain a certain level of contrast. Using tomography and 3D reconstruction techniques, we can obtain three-dimensional structural images of the cell, such as the materials' distribution. The ability to observe the behavior of the contrast agents within cells using SXT aligns perfectly with our end goal of developing CT imaging contrast agents. Compared to traditional CT, this technique allows us to observe at a more microscopic scale, revealing the three-dimensional distribution of the contrast agents after cellular uptake.

doi:10.6342/NTU202501342

Figure 3.9a and Figure 3.10 and Figure 3.11 showed the images of BxPC-3 cells incubated with Pd@Hf-EDB under SXT at 0 degree and cryo-fluorescence microscopy. Figure 3.12 showed the images of BxPC-3 cells without incubation with Pd@Hf-EDB under SXT at 0 degree and cryo-fluorescence microscopy. We used cryo-fluorescence microscopy to observe the organelles of cells frozen in liquid nitrogen. The red channel showed the acidic compartments stained with LysoTracker, the blue represented the nucleus stained with Hoechst 33342, and the green indicated the mitochondria stained with MitoTracker. Pd@Hf-EDB was phagocytosed by the cells in significant quantities. The dense yet evenly distribution of Pd@Hf-EDB with clearly visible outlines in the BxPC-3 cytoplasm (Figure 3.9a), indicating that BxPC-3 cells had a strong capacity to engulf these nanoparticles. To further observe the distribution of Pd@Hf-EDB within the cell, we performed a three-dimensional cell reconstruction in Figure 3.9a. We chose this cell as it contains three distinct Pd@Hf-EDB aggregates, making it ideal for observation. Moreover, to confirm that these aggregates are inside the cell, 3D reconstruction using SXT images from various angles and then divided the 3D image into 200 layers we performed (Figure 3.9b).

doi:10.6342/NTU202501342

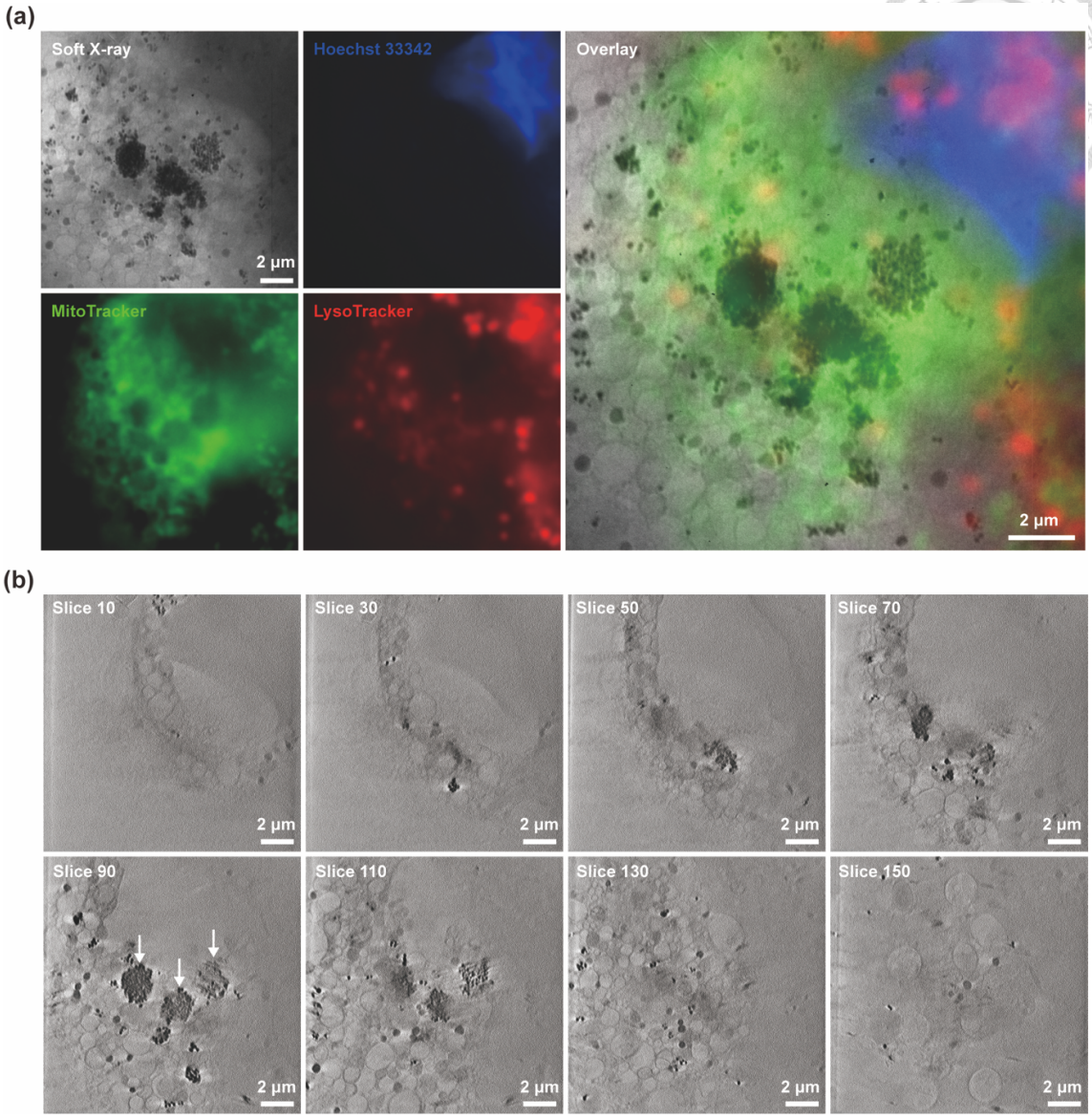

Figure 3.9. The Cellular Uptake of Pd@Hf-EDB in Soft X-ray Tomography (SXT) (a) SXT and cryo-fluorescence microscopy of the BxPC-3 cells phagocytosed Pd@Hf-EDB. The cell nucleus, mitochondria, and acidic compartment are stained by Hoechst 33342, MitoTracker, and LysoTracker, respectively. (b) The Z-stack SXT image was reconstructed into 200 slices. Arrow: Pd@Hf-EDB.

doi:10.6342/NTU202501342

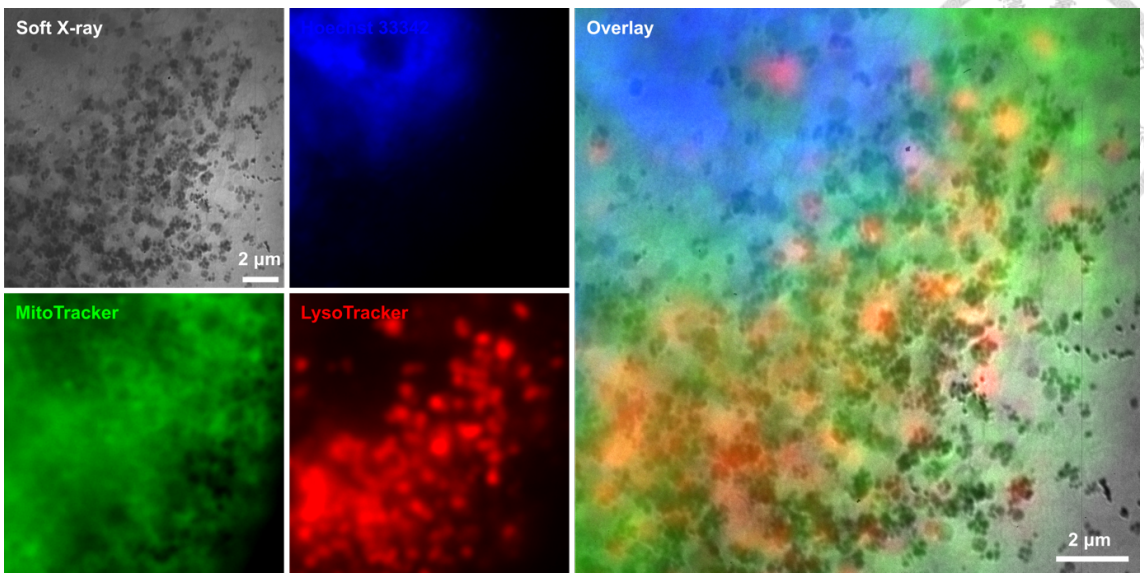

Figure 3.10. SXT and cryo-fluorescence microscopy of the BxPC-3 cells phagocytosed Pd@Hf-EDB.

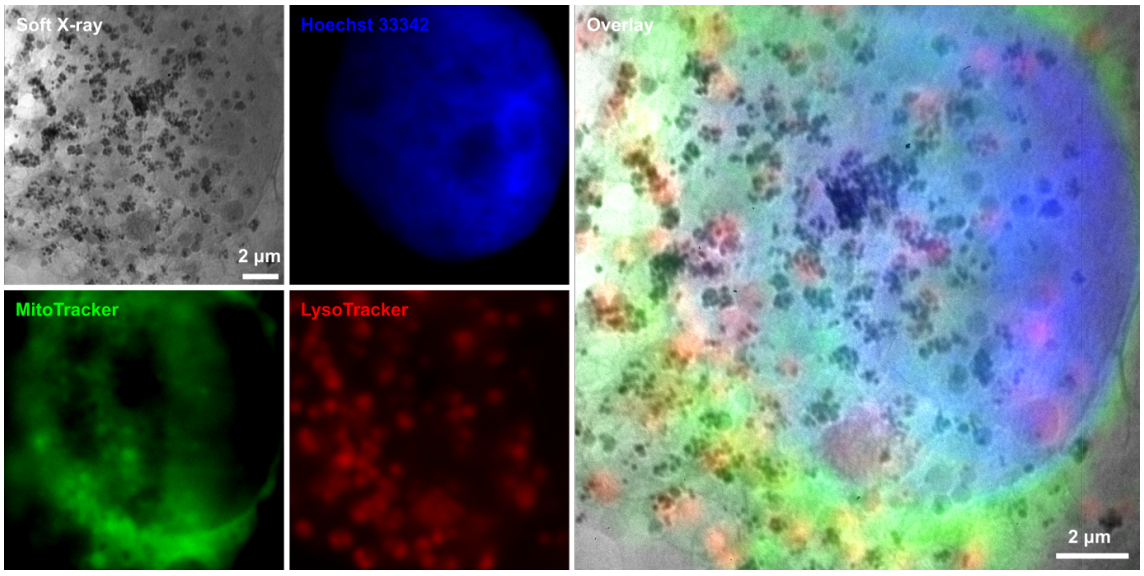

Figure 3.11. SXT and cryo-fluorescence microscopy of the BxPC-3 cells phagocytosed Pd@Hf-EDB.

doi:10.6342/NTU202501342

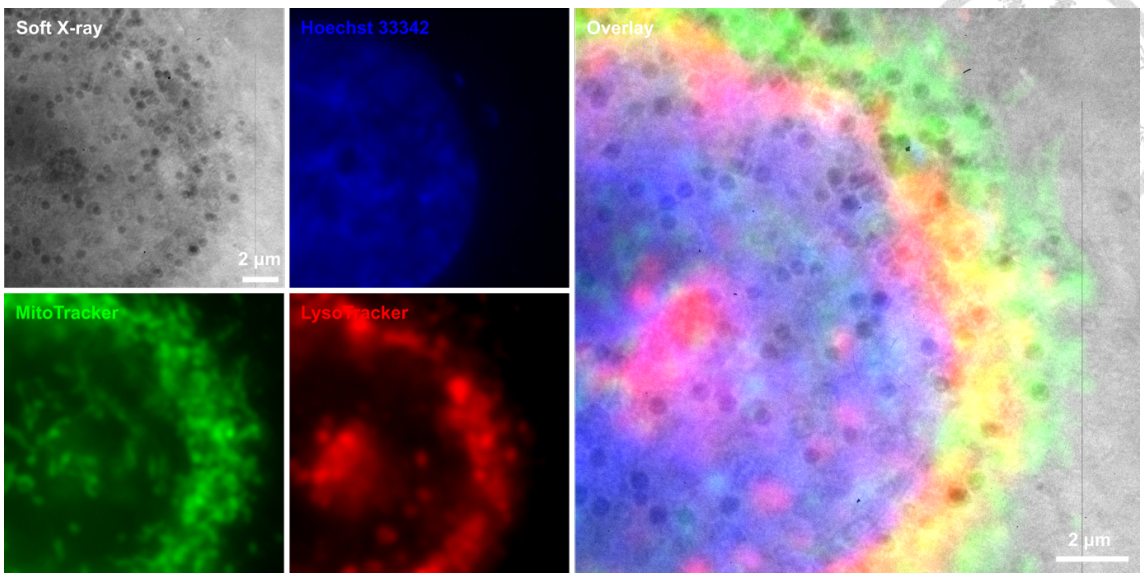

Figure 3.12. SXT and cryo-fluorescence microscopy of the BxPC-3 cells without Pd@Hf-EDB.

In Figure 3.9, layers were cut downwards from the top of the gold grid, meaning the first layer is at the top, and the last layer is near the carbon film. In the 30th slice, organelles and some Pd@Hf-EDB particles can be seen. By the 70th slice, one of the Pd@Hf-EDB aggregates appears. In the 90th layer, it becomes clearer that these three aggregates are formed by many small Pd@Hf-EDB particles, accompanied by numerous dispersed Pd@Hf-EDB particles nearby. By the 110th layer, these three aggregates begin to disappear, and by the 150th layer, the holey structures of carbon film start to appear. These results indicated that the Pd@Hf-EDB aggregates were located within the cytoplasm, with many smaller aggregates and individual Pd@Hf-EDB particles dispersed nearby.

doi:10.6342/NTU202501342

Through microscopic observation of BxPC-3 cells ingesting Pd@Hf-EDB nanoparticles, we found that Pd@Hf-EDB can be engulfed by BxPC-3 tumor cells. Many studies have mentioned that nanoparticles can accumulate in tumor cells through the Enhanced Permeability and Retention (EPR) effect. This effect presumably leads to a significant accumulation of Pd@Hf-EDB near tumors, making it an effective contrast agent.

3.6. In vitro CT imaging

To understand the capability of Hf-EDB and Pd@Hf-EDB in enhancing X-ray CT imaging and to compare them with traditional molecular contrast agents, such as iohexol, we designed an in vitro experiment. Wherein, Hf-EDB, Pd@Hf-EDB, and iohexol were separately dispersed in agarose gel at 0, 2.5, 5, 10, and 20 mg/mL concentrations to simulate a biological environment. Each mixture was then placed in Eppendorf tubes for analysis. Agarose was chosen due to its inert nature and ability to mimic the density and structure of biological tissues, providing physiologically relevant imaging results. Micro-CT imaging was performed to measure each sample's Hounsfield Unit (HU) values, quantitatively measuring the CT imaging capabilities. The HU values were calculated for each concentration using the formula $HU = 1000 \times (\mu_{sample} - \mu_{agarose}) / (\mu_{agarose} - \mu_{air})$ the

doi:10.6342/NTU202501342

symbol μ represents the linear attenuation coefficient. This coefficient indicates how much a specific material attenuates X-ray radiation as it passes through. It quantifies the probability of photon interaction with the material, which can depend on factors such as density and atomic number. Higher μ values correspond to more excellent attenuation, leading to higher HU, used to assess the different contrast in medical imaging.[62] In our calculation of HU, μ was determined using micro-CT scans. We set the reference values as follows: agarose gel was assigned a value of 0, and air was assigned a value of -1000. Additionally, we analyzed Hf-EDB, Pd@Hf-EDB, and iohexol at different concentrations dispersed within the agarose gel using Dragonfly software. By integrating their 3D images and calculating the average, we obtained the corresponding μ values for each group. Linear fitting of the CT value as a function of Hf-EDB, Pd@Hf-EDB, and iohexol concentrations in agarose gel were plotted to compare the imaging capabilities (Figure 3.13a). Phantom CT contrast images of Hf-EDB, Pd@Hf-EDB, and iohexol at different concentrations are shown in Figure 3.13b.

doi:10.6342/NTU202501342

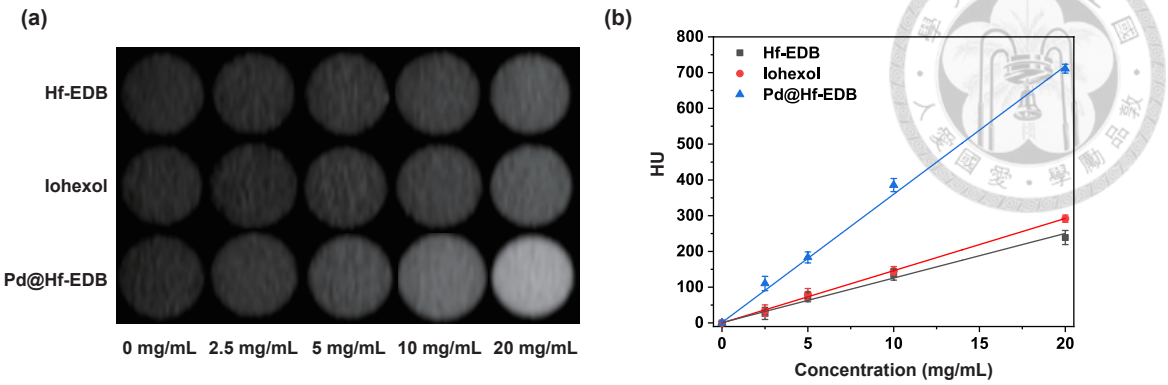

Figure 3.13. (a) In vitro phantom CT contrast images of Hf-EDB, iohexol, and Pd@Hf-EDB at different concentrations: 0, 2.5, 5, 10, 20 mg/mL. (b) CT values of Hf-EDB, iohexol, and Pd@Hf-EDB at different concentrations: 0, 2.5, 5, 10, and 20 mg/mL.

The results showed that Hf-EDB and iohexol exhibited similar CT imaging capabilities, as nearly overlapping attenuation curves indicated. This similarity could be attributed to hafnium's high X-ray absorption properties (Z = 72) and iodine (Z = 53), which have high electron densities. In Hf-EDB, hafnium makes up about 38% by weight (from ICP-OES), while in iohexol, iodine accounts for approximately 46% by weight. These comparable weight percentages likely contributed to their similar imaging performance. This similarity suggested that Hf-EDB, like iohexol, provided a baseline level of contrast enhancement suitable for many imaging applications. Furthermore, Pd@Hf-EDB demonstrated a significantly higher imaging capability. The attenuation

doi:10.6342/NTU202501342

curve for Pd@Hf-EDB was substantially above those of Hf-EDB and iohexol, with HU values approximately three times greater than those of iohexol at equivalent concentrations. The enhanced performance of Pd@Hf-EDB can be attributed to the presence of palladium, which may increase the X-ray attenuation properties because palladium (Z = 46) accounts for approximately 26% by weight in Pd@Hf-EDB. This increased attenuation is crucial for improving the contrast in CT images, potentially allowing for more precise and more detailed visualization of tissues.

While Iohexol often suffers rapid renal clearance and limited X-ray absorption capacity. Pd@Hf-EDB nanoparticles offer several advantages including enhanced accumulation in tumor tissues due to the EPR effect, which provides better contrast in cancer imaging,[63] longer blood circulation times, allowing for prolonged imaging windows.[64] Additionally, Pd@Hf-EDB can also be modified on the surface with targeting ligands to improve specificity for specific tissues or tumors thereby highlighting the potential of this novel materials i.e., Pd@Hf-EDB nanoparticles as a promising candidate as CT contrast agent.

doi:10.6342/NTU202501342

3.7. In vitro PA imaging

To understand the capacity of Pd@Hf-EDB nanoparticles as an efficient PA imaging contrast agent, we first measured the Pd@Hf-EDB suspensions at various concentrations by ultraviolet-visible/near-infrared (UV-vis/NIR) absorption spectroscopy. The optical absorption spectra reveal a broad absorption band extending from 300 to 1300 nm (Figure 3.8b), with a particular focus on the near-infrared (NIR) region beyond 700 nm (Figure 3.14a). Light in this range has a high tissue penetration rate, making it suitable for medical applications like photothermal therapy. Pd@Hf-EDB demonstrated a significant absorption level within this NIR region, which gradually decreased as the wavelength increased.[65] For different concentrations (25, 50, 100, and 200 ppm), the normalized absorption intensity per characteristic cell length (A/L) is measured at specific wavelengths of 750, 800, 850, 900, 950, and 975 nm (Figure 3.14b). Applying the Lambert–Beer law, represented as $A/L = \alpha C$, where A denotes absorbance intensity, L represents the cell length, α is the extinction coefficient, and C is the concentration, a linear relationship is observed between A/L and concentration, allowing for the calculation of extinction coefficients at the designated wavelengths (Table 3.3).

doi:10.6342/NTU202501342

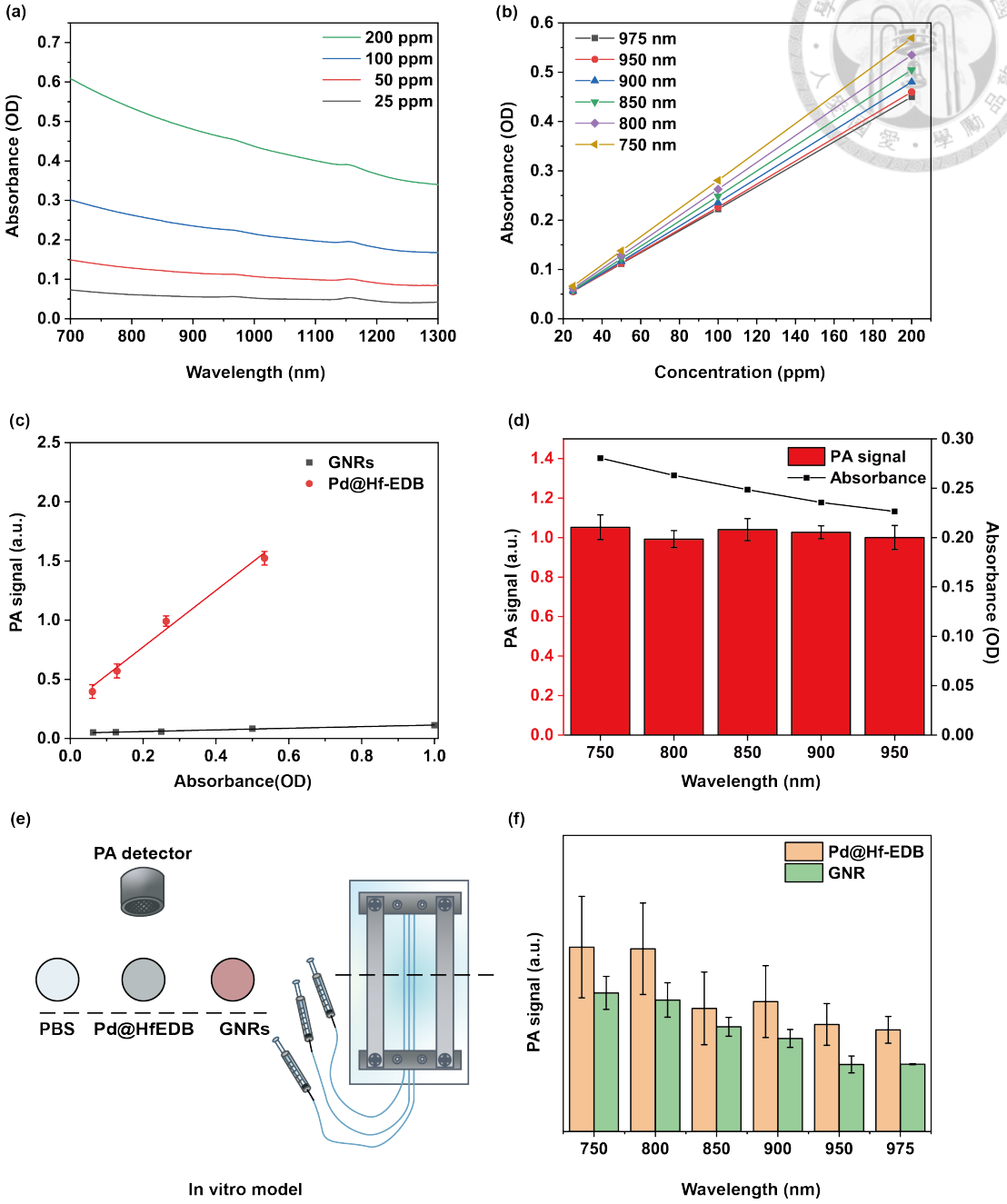

Figure 3.14. *In vitro* PA imaging of Pd@Hf-EDB nanoparticles. (a) Absorbance spectra of Pd@Hf-EDB dispersed in water at different concentrations. (b) The absorbance of Pd@Hf-EDB to varying concentrations for λ = 750, 800, 850, 900, 950, 975 nm. (c) PA signal of Pd@Hf-EDB and GNRs for different optical densities at 800 nm. (d) PA signal

doi:10.6342/NTU202501342

and absorbance of Pd@Hf-EDB at 100 ppm for different wavelengths. (e) In vitro model scheme for simulating blood vessels. (f) PA signal of Pd@Hf-EDB and GNRs at 100 ppm for different wavelengths.

Table 3.3. Extinction coefficients at different wavelengths

λ (nm)	***α*** **($Lg^{-1}cm^{-1}$)**
750 nm	2.9
800 nm	2.7
850 nm	2.6
900 nm	2.4
950 nm	2.3
975 nm	2.3

To evaluate the PA performance of Pd@Hf-EDB compared to gold nanorods (GNRs) as PA contrast agents, we conducted an in vitro experiment. We dispersed varying concentrations of Pd@Hf-EDB and GNRs in 100 × 20 mm cell culture dishes, using 25, 50, 100, and 200 ppm concentrations for Pd@Hf-EDB. The optical density (OD) values were calculated based on the calibration line shown in Figure 3.14b, while the OD for GNRs was obtained using UV-Vis/NIR measurements. A coupling gel was applied

doi:10.6342/NTU202501342

underneath the ultrasound receiver and then attached to the liquid surface to measure the PA signals. To quantitatively compare the PA signal generation ability of Pd@Hf-EDB and GNRs, we analyzed the slopes of PA signal versus OD values at 800 nm from Figure 3.14c. The slope for Pd@Hf-EDB was calculated to be 2.38, while for GNRs it was only 0.70, indicating that Pd@Hf-EDB exhibits a significantly stronger correlation between optical absorption and PA output signal. This suggests that Pd@Hf-EDB has a more efficient conversion of absorbed light into acoustic energy. The higher slope can be attributed to the strong interband transition of Pd nanoparticles in the NIR region and their enhanced photothermal stability, which helps retain consistent PA signal output under prolonged excitation without structural degradation. This suggests that Pd@Hf-EDB has superior PA contrast capabilities relative to GNRs, and the detection limit for Pd@Hf-EDB was determined to be as low as OD = 0.061 (equivalent to 25 ppm), highlighting its exceptional performance as a PA contrast agent. Additionally, Figure 3.14d illustrated the PA signals of Pd@Hf-EDB at 100 ppm across different wavelengths, revealing a trend similar to that observed in UV-Vis/NIR measurements, with consistent PA signals in the NIR region. This correlation further reinforced the potential of Pd@Hf-EDB as an effective PA contrast agent, particularly in the NIR region, which is crucial for deep tissue imaging.

doi:10.6342/NTU202501342

Moreover, to simulate the vascular environment, the Pd@Hf-EDB and GNRs were dispersed in solutions at a concentration of 100 ppm, and each mixture was then injected into polyethylene tubing with an inner diameter of 0.38 mm using insulin syringes (Figure 3.14e). The PA signals were then measured using a custom-made Dual-mode US/PA imaging system from the NHRI Liao lab across the specified wavelengths of 750, 800, 850, 900, 950, and 975 nm. This wavelength range is selected based on the high tissue penetration of NIR light. The PA signals were analyzed, focusing on the longitudinal section of the simulated vascular model. The integrals of image value within the region of interest (ROI) were recorded as the PA signal for each material.

The results showed that under 800 nm laser irradiation, the PA signal intensity of Pd@Hf-EDB at 100 ppm was found to be 1.38 times higher than that of GNRs at the same concentration (Figure 3.14f). Additionally, PA signal trends observed for both Pd@Hf-EDB and GNR indicated a decrease with increasing wavelength (Figure 3.14f). This trend aligns with the results obtained from UV-Vis/NIR spectroscopy. When optically absorbing materials like Pd@Hf-EDB and GNR are exposed to laser pulses shorter than the time required for thermal energy transport, they undergo transient thermoelastic expansion, producing a subsequent PA pressure wave. During this thermal

doi:10.6342/NTU202501342

expansion, the efficiency of converting light energy into a PA pressure wave is crucial for generating the PA signal. This conversion efficiency is primarily determined by the optical absorber's light absorbance, photothermal conversion efficiency, and thermal properties such as heat capacity and thermal conductivity.[66]

The enhanced PA performance of Pd@Hf-EDB compared to GNRs can be attributed to two key factors: (i) the broader and stronger NIR absorption profile of Pd nanoparticles, which leads to more efficient light-to-heat conversion, and (ii) the MOF framework of Pd@Hf-EDB, which may stabilize the embedded Pd nanoparticles and minimizes photothermal degradation or morphological deformation that GNRs commonly experience under prolonged laser exposure. These characteristics not only explain the superior PA signal output of Pd@Hf-EDB but also clarify why its PA signal trend closely follows its UV-Vis/NIR absorbance spectrum. In contrast, the lower PA signals observed in GNRs may result from scattering losses or instability during excitation. In conclusion, these findings support that Pd@Hf-EDB is more effective and stable as a PA imaging agent in the NIR region, reinforcing its strong potential for biomedical imaging applications.

doi:10.6342/NTU202501342

3.8. In vivo PA imaging

In this work, in vivo PA and CT imaging experiments were conducted using Pd@Hf-EDB as a CT/PA dual-modal contrast agent. We employed a xenograft tumor model in nude mice, which was established by subcutaneously implanting BxPC-3 cancer cells. Once the tumor size reached approximately 150 mm^3, we calculated the required amount of Pd@Hf-EDB based on the tumor size to achieve a concentration of 100 ppm. The compound was dispersed in 100 μL of PBS and injected subcutaneously near the tumor. About 30 minutes later, we used a PA instrument, initially utilizing ultrasound to locate the tumor. We then activated the laser to measure the PA signal and scanned a 3D image of the tumor area, approximately 1.5 cm in length, 1.3 cm in width, and 6 cm in depth. The length was divided into 20 sections to obtain cross-sectional views using a wavelength of 750 nm. The results demonstrated a strong PA signal contrast of our material within the tumor, which overlapped with the tumor location in the ultrasound images (Figure 3.15a, b).

doi:10.6342/NTU202501342

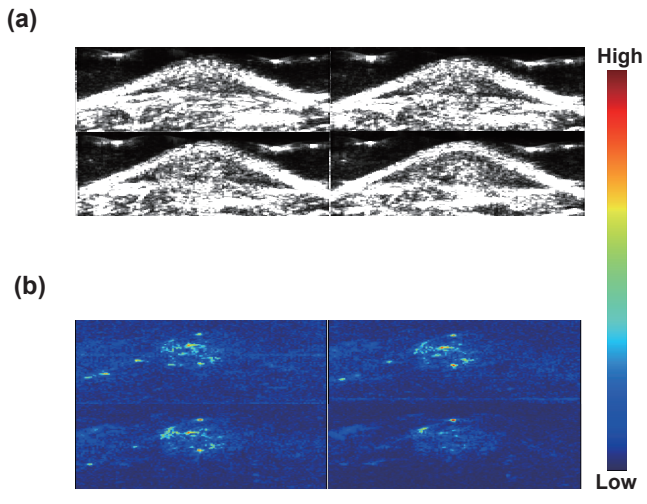

Figure 3.15. *In vivo* PA performance of Pd@Hf-EDB nanoparticles. (a) Ultrasound images of the BxPC-3 cells in the xenografted tumor in the nude mice. (b) A 3D sectional view of the PA images of the tumor at different positions post-injection of Pd@Hf-EDB. (c) A 3D sectional view of the CT images of the tumor at different positions post-injection of Pd@Hf-EDB.

After the PA experiment, we conducted the CT experiment using a micro-CT on the entire mouse body with a PET/SPECT/CT Tri-Modality Imaging System (GAMMA MEDICA-IDEAS, FLEX Triumph) at an X-ray tube voltage of 50 kVp. Using Fiji software, we examined the 3D cross-sectional images of the tumor (Figure 3.15c). The bright high-contrast spots represent our material, Pd@Hf-EDB. Areas outside the bright spots did not show the obvious contrast of the material. We speculate this is due to two reasons: first, the dosage used was based on cell viability tests, and micro-CT requires a

doi:10.6342/NTU202501342

higher dosage for clear contrast. Thus, the bright spots may result from the aggregation of Pd@Hf-EDB due to uneven dispersion. Second, the energy of the micro-CT X-rays differs from the detectable energy range for metal particles, as it primarily aims for contrast in soft tissue. This is a common challenge for metal particle contrast agents, as different metals require specific X-ray energies.[43]

Although the subcutaneous injection did not allow for uniform distribution of the contrast agent in the bloodstream, the results showed a significant PA and CT signal. Combined with the enhanced permeability and retention (EPR) effect of the tumor region for nanoparticles, the contrast agent can accumulate more uniformly.[63]

3.9. Comparative analysis with leading technologies

In recent years, many research groups have begun to explore the application of MOFs.[67] On the other hand, traditional inorganic nanocarriers such as iron oxide (Fe_3O_4) nanoparticles have been widely utilized in MRI diagnostics due to their good magnetic properties and biocompatibility.[68] However, these nanoparticles often face challenges related to difficulties in surface modification,[69] limited drug loading capacity, and issues in achieving precise drug release control.[70] Additionally, gold nanoparticles, although exhibiting outstanding contrast performance in CT imaging, are limited in clinical

doi:10.6342/NTU202501342

application due to potential cellular toxicity at high dosages and insufficient biodegradability.[71]

In comparison, MOFs can efficiently load various imaging probes and allow facile tuning of physicochemical properties by selecting appropriate metal ions or organic linkers. Their easily functionalizable surfaces, particularly ion clusters capable of coordinating biomolecules, further enhance tumor-targeting specificity, which is a significant advantage over non-MOF materials.[67]

Many current studies on MOF-based contrast agents have focused primarily on MRI applications.[72] This is largely attributable to the outstanding magnetic properties and easily tunable structures of MOFs, which significantly enhance MRI image contrast. For instance, Wang et al.[73] introduced that Gd^{3+}- or Mn^{2+}-based MOFs have excellent performance as MRI contrast agents. In addition, some researches focus on MOFs as contrast agents for CT imaging; for example, K. E. deKrafft et al.[74] developed Zr and Hf-based MOFs for use as contrast agents in CT imaging.

However, studies employing MOFs for dual-modal imaging applications are relatively scarce compared to conventional non-MOF materials. For example, Rieter et

doi:10.6342/NTU202501342

al.[75] reported on nanoscale Gd^{3+}-based MOFs as multimodal imaging contrast agent for combining MRI with optical imaging. Tian et al.[76] integrated gold nanoparticles with Gd-based MOFs to develop a dual-modal contrast agent for CT and MRI imaging. In particular, these MOFs dual-modal contrast agents have rarely involved PAI. Compared to relatively common CT/MRI dual-modal imaging combinations, Pd@Hf-EDB as a CT/PA dual-modal contrast agent demonstrates several distinct benefits. Although MRI provides excellent soft-tissue contrast, it suffers from relatively low sensitivity and long scanning times.[77] On the other hand, PAI combines the high molecular sensitivity of optical imaging with real-time monitoring of molecular and functional information within the tumor microenvironment,[28] such as tumor angiogenesis,[29] oxygenation, and hypoxic conditions,[13, 30] which information that traditional MRI techniques usually cannot provide quickly and sensitively. Furthermore, combining CT and PAI provides effective complementary information with anatomical details in CT imaging. Thus, the combination of CT and PAI imaging technology is highly suitable for efficient tumor diagnosis and localization applications.

Overall, Pd@Hf-EDB combines the advantages of MOFs with the dual-modal imaging capabilities of CT and PAI, marking the first reported application of nanoscale Hf-based MOFs in these CT/PA dual-modal technologies.

doi:10.6342/NTU202501342

Table 3.4. Comparative analysis of Pd@Hf-EDB with leading imaging technologies

Materials	MOF	Dual-modal	Imaging types	Advantages	Disadvantages	Ref.
Fe3O4 NPs	No	No	MRI	Good biocompatibility; Good magnetic properties	Limiting drug loading; Surface modification challenges	[68]
Gold NPs	No	No	CT	High CT contrast performance	Limiting drug loading; High cost	[69]
Gd or Mn-based MOF	Yes	No	MRI	Tunable structures; Good MRI contrast	Insufficient biodegradability; Single modality	[73]
Zr or Hf-based MOF	Yes	No	CT	Tunable structures; Good CT contrast	Single modality; High cost	[74]
Gd-based MOF	Yes	Yes	MRI/optical	Dual-modality; Tunable structures	Low sensitivity; High cost	[75]
Gold NPs/Gd-based MOF	Yes	Yes	CT/MRI	Dual-modality; Tunable structures	Low sensitivity; High cost	[76]
Pd@Hf-EDB	Yes	Yes	PA/CT	Dual-modality; High sensitivity	Requires further investigations to ensure targeted binding	This work

Table 3.5. Comparative analysis of Pd@Hf-EDB with other dual-modal imaging materials

Materials	Imaging types	Advantages	Disadvantages	Ref.
DOTA–QD–RGD	PET/NIRF	High specificity; Low toxicity	Low in vivo targeting efficiency; Surface modification challenges	[15]
Gd/CuS@PEI-FA-PS NGs	MR/PA	Effective photothermal performance; Excellent dispersion	Synthetic complexity; Unclear stability	[16]
GM-PET Fusion	MRI/PET	Detailed structural information; Enhanced functional diagnosis	Synthetic complexity; Unclear stability	[17]

doi:10.6342/NTU202501342

Au-AgI core/shell	CT/PA	Effective dual-modal imaging; Good stability	Complex synthesis; Surface modification challenges	[36]
Gd-based MOF	MRI/optical	High structural tunability; Tunable optical properties	Low sensitivity; Synthetic limitations	[75]
Gold NPs/Gd-based MOF	CT/MRI	High structural tunability; Good stability	Complex synthesis; High cost	[76]
Pd@Hf-EDB	PA/CT	High structural tunability; High sensitivity	High cost; Equipment limitations	This work

3.10. Study limitations

In this study, we focused on the design and application of MOF-based nanomaterials and demonstrated the potential of Pd@Hf-EDB as a dual-modal contrast agent for CT and PAI. We have proved its imaging capabilities through preliminary subcutaneous injection models. However, in clinical application, contrast agents are typically administered intravenously. The MOF's framework of Pd@Hf-EDB offers the advantage of easy surface modification; specifically, ion clusters on the framework can be utilized to coordinate targeting molecules containing carboxyl functional groups,[78] thereby enhancing tumor specificity. When combined with cancer treatment, this approach also has the potential for theranostic applications.

However, before such applications can be realized, assessing the ethical considerations of using Pd@Hf-EDB as a contrast agent is crucial. Because Pd@Hf-EDB

doi:10.6342/NTU202501342

comprises metal components (Hf and Pd) and organic linkers (H_2EDB), their long-term biological interactions and potential toxic effects remain insufficiently understood. The metabolism and excretion pathways of Pd@Hf-EDB are primarily influenced by its nanoparticulate nature. MOFs, such as Hf-EDB, typically undergo gradual degradation within physiological environments, releasing their metal components (Hf and Pd) over time. Hf as a high-Z element, generally exhibits low toxicity and limited bioavailability, consistent with existing literature on hafnium-based materials used clinically or in advanced biomedical research.[20] However, Pd necessitates careful consideration due to its potential for toxicity upon prolonged exposure.[79] Nanoparticles administered intravenously or subcutaneously are often subject to uptake by the reticuloendothelial system (RES), predominantly in organs such as the liver, spleen, and kidneys.[35] Accumulation of Pd@Hf-EDB nanoparticles in these organs may lead to risks of toxicity if Pd ions are excessively released. Therefore, longitudinal studies investigating biodistribution, accumulation kinetics, and clearance mechanisms of Pd@Hf-EDB are essential for thorough safety evaluation. Future work should involve histological analysis and elemental quantification in vital organs at multiple time points post-administration to assess potential chronic effects.

doi:10.6342/NTU202501342

Comparatively, clinically utilized contrast agents, such as iodine-based agents for CT and gadolinium-based agents for MRI, often exhibit rapid renal excretion and minimal long-term accumulation. However, these agents also present significant limitations, including nephrotoxicity and potential nephrogenic systemic fibrosis.[46, 80] Pd@Hf-EDB nanoparticles, due to their size and surface properties, may offer a more extended viewing time and reduced acute toxicity compared to these traditional agents. Nevertheless, comprehensive toxin analysis is necessary to conclusively determine their relative safety.

In addition to patient safety, the environmental impacts associated with the synthesis, usage, and disposal of Pd@Hf-EDB must be carefully considered. As previously mentioned, the synthesis involves potentially hazardous solvents such as dimethylformamide (DMF), metal ions (Hf and Pd), and organic linkers (H_2EDB). According to recent literature on MOFs, the presence of heavy metals and organic solvents used during synthesis can lead to significant environmental toxicity if not managed properly. For instance, solvents such as DMF are known to pose risks due to their toxicity and persistence in the environment.[81] Additionally, metal ions such as Pd^{2+} and Hf^{4+} tend to be oxidized to form metal oxide, which may have toxic effects in our environment.[81]

doi:10.6342/NTU202501342

Recent studies highlight the importance of adopting green synthesis techniques to mitigate these environmental concerns. Sustainable synthesis strategies involving water solvents, supercritical liquids, ionic liquids, or bioderived solvents have been proposed as safer alternatives to conventional hazardous solvents.[82] Although the current synthesis of Pd@Hf-EDB requires the use of DMF, we can move towards developing alternative synthesis methods that replace DMF with safer and more sustainable solvents.

Furthermore, proper procedures for disposal, recycling, and regeneration processes such as solvent exchange, thermal activation, vacuum treatment, and supercritical CO_2 methods have been recommended to enhance sustainability in MOF usage.[81] These methods can help minimize hazardous waste generation and reduce contamination risks associated with MOF disposal. Thus, it is essential for researchers involved with Pd@Hf-EDB to adopt sustainable synthesis methods and develop appropriate recycling and disposal strategies to minimize potential ecological harm and to promote environmentally friendly practices in MOF research and applications.

doi:10.6342/NTU202501342

4. Conclusions

In summary, we successfully synthesized Hf-EDB and loaded Pd nanoparticles inside the pores of Hf-EDB to attain Pd@Hf-EDB nanopartilces. The biocompatibility of Pd@Hf-EDB was confirmed, maintaining 85% and 90% cell viability in BxPC-3 and RAW264.7 cells, respectively, at 100 μg/mL. Through SXT images of BxPC-3 cells ingesting Pd@Hf-EDB nanoparticles, we found that Pd@Hf-EDB can be readily engulfed by BxPC-3 tumor cells. A comparison with iohexol for in vitro CT imaging revealed that Hf-EDB possesses similar CT imaging capabilities, attributable to its high hafnium content. However, Pd@Hf-EDB exhibited superior imaging performance, with attenuation values approximately three times greater than iohexol due to its significant palladium content enhancing X-ray attenuation. For in vitro PA imaging, Pd@Hf-EDB outperformed gold nanorods (GNRs), showing higher efficacy in the NIR region. This efficiency is improved by Pd@Hf-EDB's structural stability and absorption properties, making it more effective than GNR, which may suffer from degradation or scattering under prolonged excitation. The in vivo results demonstrated a strong PA and CT signal contrast of our material within the tumor, which overlapped with the tumor location in the ultrasound images. Overall, Pd@Hf-EDB possesses dual-modal capabilities, biocompatibility, and superior imaging performance, highlighting its potential for

doi:10.6342/NTU202501342

advanced imaging applications and offering more precise visualization and enhanced diagnostic accuracy.

doi:10.6342/NTU202501342

5. References

[1] Torigian, D. A.; Huang, S. S.; Houseni, M.; Alavi, A., Functional imaging of cancer with emphasis on molecular techniques. *CA Cancer J. Clin.* **2007**, *57*, 206-224.

[2] Kunjachan, S.; Ehling, J.; Storm, G.; Kiessling, F.; Lammers, T., Noninvasive imaging of nanomedicines and nanotheranostics: principles, progress, and prospects. *Chem. Rev.* **2015**, *115*, 10907-10937.

[3] Jiang, H.-Y.; Chen, J.; Xia, C.-C.; Cao, L.-K.; Duan, T.; Song, B., Noninvasive imaging of hepatocellular carcinoma: From diagnosis to prognosis. *World J. Gastroenterol.* **2018**, *24*, 2348.

[4] Fass, L., Imaging and cancer: a review. *Mol. Oncol.* **2008**, *2*, 115-152.

[5] Koo, V.; Hamilton, P.; Williamson, K., Non-invasive in vivo imaging in small animal research. *Anal. Cell. Pathol.* **2006**, *28*, 127-139.

[6] Vogel, A.; Chernomordik, V. V.; Riley, J. D.; Hassan, M.; Amyot, F.; Dasgeb, B.; Demos, S. G.; Pursley, R.; Little, R. F.; Yarchoan, R., Using noninvasive multispectral imaging to quantitatively assess tissue vasculature. *J. Biomed. Opt.* **2007**, *12*, 051604-051604-13.

[7] Derlin, T.; Grünwald, V.; Steinbach, J.; Wester, H.-J.; Ross, T. L., Molecular imaging in oncology using positron emission tomography. *Dtsch. Arztebl. Int.* **2018**, *115*, 175.

[8] Jansen, R. W.; van Amstel, P.; Martens, R. M.; Kooi, I. E.; Wesseling, P.; de Langen, A. J.; Menke-Van der Houven, C. W.; Jansen, B. H.; Moll, A. C.; Dorsman, J. C., Non-invasive tumor genotyping using radiogenomic biomarkers, a systematic review and oncology-wide pathway analysis. *Oncotarget* **2018**, *9*, 20134.

[9] Xiao, Y.-D.; Paudel, R.; Liu, J.; Ma, C.; Zhang, Z.-S.; Zhou, S.-K., MRI contrast agents: Classification and application. *Int. J. Mol. Med.* **2016**, *38*, 1319-1326.

[10] Yin, Q.; Yap, F. Y.; Yin, L.; Ma, L.; Zhou, Q.; Dobrucki, L. W.; Fan, T. M.; Gaba, R. C.; Cheng, J., Poly (iohexol) nanoparticles as contrast agents for in vivo X-ray computed tomography imaging. *J. Am. Chem. Soc.* **2013**, *135*, 13620-13623.

[11] Wadas, T. J.; Wong, E. H.; Weisman, G. R.; Anderson, C. J., Coordinating radiometals of copper, gallium, indium, yttrium, and zirconium for PET and SPECT imaging of disease. *Chem. Rev.* **2010**, *110*, 2858-2902.

[12] Chuang, Y.-C.; Hsia, Y.; Chu, C.-H.; Maharajan, S.; Hsu, F.-C.; Lee, H.-L.; Chiou, J. F.; Ch'ang, H.-J.; Liao, L.-D.; Lo, L.-W., Photothermal temperature-modulated cancer metastasis harnessed using proteinase-triggered assembly of near-infrared

doi:10.6342/NTU202501342

II photoacoustic/photothermal nanotheranostics. *ACS Appl. Interfaces* **2024**, *16*, 40611-40627.

[13] Wang, Y.; Jhang, D.-F.; Tsai, C.-H.; Chiang, N.-J.; Tsao, C.-H.; Chuang, C.-C.; Chen, L.-T.; Chang, W.-S. W.; Liao, L.-D., In vivo assessment of hypoxia levels in pancreatic tumors using a dual-modality ultrasound/photoacoustic imaging system. *Micromachines* **2021**, *12*, 668.

[14] Sivasubramanian, M.; Wang, Y.; Lo, L.-W.; Liao, L.-D., Personalized cancer therapeutics using photoacoustic imaging-guided sonodynamic therapy. *IEEE Trans. Ultrason. Ferroelectr. Freq. Control* **2023**, *70*, 1682-1690.

[15] Cai, W.; Chen, K.; Li, Z.-B.; Gambhir, S. S.; Chen, X., Dual-function probe for PET and near-infrared fluorescence imaging of tumor vasculature. *J. Nucl. Med.* **2007**, *48*, 1862-1870.

[16] Zhang, C.; Sun, W.; Wang, Y.; Xu, F.; Qu, J.; Xia, J.; Shen, M.; Shi, X., Gd-/CuS-loaded functional nanogels for MR/PA imaging-guided tumor-targeted photothermal therapy. *ACS Appl. Mater. Interfaces* **2020**, *12*, 9107-9117.

[17] Song, J.; Zheng, J.; Li, P.; Lu, X.; Zhu, G.; Shen, P., An effective multimodal image fusion method using MRI and PET for Alzheimer's disease diagnosis. *Front. Digital Health* **2021**, *3*, 637386.

[18] Liu, Y.; Li, J.; Chen, M.; Chen, X.; Zheng, N., Palladium-based nanomaterials for cancer imaging and therapy. *Theranostics* **2020**, *10*, 10057.

[19] Kim, J.; Piao, Y.; Hyeon, T., Multifunctional nanostructured materials for multimodal imaging, and simultaneous imaging and therapy. *Chem. Soc. Rev.* **2009**, *38*, 372-390.

[20] Lusic, H.; Grinstaff, M. W., X-ray-computed tomography contrast agents. *Chemical reviews* **2013**, *113*, 1641-1666.

[21] Cormode, D. P.; Naha, P. C.; Fayad, Z. A., Nanoparticle contrast agents for computed tomography: a focus on micelles. *Contrast Media Mol. Imaging* **2014**, *9*, 37-52.

[22] Shi, J.; Tang, Y.; Yao, J., Advances in super-resolution photoacoustic imaging. *Quant. Imaging Med. Surg.* **2018**, *8*, 724.

[23] Beard, P., Biomedical photoacoustic imaging. *Interface Focus* **2011**, *1*, 602-631.

[24] Wang, L. V.; Gao, L., Photoacoustic microscopy and computed tomography: from bench to bedside. *Annu. Rev. Biomed. Eng.* **2014**, *16*, 155-185.

[25] Upputuri, P. K.; Pramanik, M., Recent advances in photoacoustic contrast agents for in vivo imaging. *Wiley Interdiscip. Rev. Nanomed. Nanobiotechnol.* **2020**, *12*, e1618.

[26] Yuan, B.; Rychak, J., Tumor functional and molecular imaging utilizing ultrasound and ultrasound-mediated optical techniques. *Am. J. Pathol.* **2013**, *182*,

doi:10.6342/NTU202501342

305-311.

[27] Weber, J.; Beard, P. C.; Bohndiek, S. E., Contrast agents for molecular photoacoustic imaging. *Nat. Methods* **2016**, *13*, 639-650.

[28] Gargiulo, S.; Albanese, S.; Mancini, M., State-of-the-Art Preclinical Photoacoustic Imaging in Oncology: Recent Advances in Cancer Theranostics. *Contrast Media Mol. Imaging* **2019**, *2019*, 5080267.

[29] Cai, W.; Chen, X., Multimodality molecular imaging of tumor angiogenesis. *J. Nucl. Med.* **2008**, *49*, 113S-128S.

[30] Li, M.-L.; Oh, J.-T.; Xie, X.; Ku, G.; Wang, W.; Li, C.; Lungu, G.; Stoica, G.; Wang, L. V., Simultaneous molecular and hypoxia imaging of brain tumors in vivo using spectroscopic photoacoustic tomography. *Proc. IEEE* **2008**, *96*, 481-489.

[31] Wang, S.; Lin, J.; Wang, T.; Chen, X.; Huang, P., Recent advances in photoacoustic imaging for deep-tissue biomedical applications. *Theranostics* **2016**, *6*, 2394.

[32] Jung, D.; Park, S.; Lee, C.; Kim, H., Recent progress on near-infrared photoacoustic imaging: imaging modality and organic semiconducting agents. *Polymers* **2019**, *11*, 1693.

[33] Liu, Y.; Nie, L.; Chen, X., Photoacoustic molecular imaging: from multiscale biomedical applications towards early-stage theranostics. *Trends Biotechnol.* **2016**, *34*, 420-433.

[34] Hainfeld, J.; Slatkin, D.; Focella, T.; Smilowitz, H., Gold nanoparticles: a new X-ray contrast agent. *Br. J. Radiol.* **2006**, *79*, 248-253.

[35] Cho, E. C.; Glaus, C.; Chen, J.; Welch, M. J.; Xia, Y., Inorganic nanoparticle-based contrast agents for molecular imaging. *Trends Mol. Med.* **2010**, *16*, 561-573.

[36] Orza, A.; Yang, Y.; Feng, T.; Wang, X.; Wu, H.; Li, Y.; Yang, L.; Tang, X.; Mao, H., A nanocomposite of Au-AgI core/shell dimer as a dual-modality contrast agent for x-ray computed tomography and photoacoustic imaging. *Med. Phys.* **2016**, *43*, 589-599.

[37] Hsu, C.-H.; Chen, W.-L.; Hsieh, M.-F.; Gu, Y.; Wu, K. C.-W., Construction of magnetic Fe3O4@ NH2-MIL-100 (Fe)-C18 with excellent hydrophobicity for effective protein separation and purification. *Sep. Purif. Technol.* **2022**, *301*, 121986.

[38] Tan, J.-X.; Chen, Z.-Y.; Chen, C. H.; Hsieh, M.-F.; Lin, A. Y.-C.; Chen, S. S.; Wu, K. C.-W., Efficient adsorption and photocatalytic degradation of water emerging contaminants through nanoarchitectonics of pore sizes and optical properties of zirconium-based MOFs. *J. Hazard. Mater.* **2023**, *451*, 131113.

[39] Li, S.-W.; Hsieh, M.-F.; Hong, T.; Chen, P.; Osada, K.; Liu, X.; Aoki, I.; Yu, J.; Wu, K. C.-W.; Cabral, H., Block Copolymer-Stabilized Metal-Organic

doi:10.6342/NTU202501342

Framework Hybrids Loading Pd Nanoparticles Enable Tumor Remission Through Near-Infrared Photothermal Therapy. *Adv. NanoBiomed Res.* **2024**, *4*, 2300107.

[40] Gole, B.; Sanyal, U.; Banerjee, R.; Mukherjee, P. S., High loading of Pd nanoparticles by interior functionalization of MOFs for heterogeneous catalysis. *Inorg. Chem.* **2016**, *55*, 2345-2354.

[41] Yu, Y.-S.; Chen, M.-H.; Chen, H.-M.; Hsu, C.-H.; Su, W.-P.; Wu, K. C.-W., Dual-Sensitization of X-Ray and Near-Infrared Based on Pd-Loaded Metal-Organic Framework for Radiation-Photothermal Combined Cancer Therapy. *Available at SSRN 4176677*.

[42] Xiao, J.-W.; Fan, S.-X.; Wang, F.; Sun, L.-D.; Zheng, X.-Y.; Yan, C.-H., Porous Pd nanoparticles with high photothermal conversion efficiency for efficient ablation of cancer cells. *Nanoscale* **2014**, *6*, 4345-4351.

[43] Aslan, N.; Ceylan, B.; Koç, M. M.; Findik, F., Metallic nanoparticles as X-Ray computed tomography (CT) contrast agents: A review. *J. Mol. Struct.* **2020**, *1219*, 128599.

[44] Jackson, P. A.; Rahman, W. N. W. A.; Wong, C. J.; Ackerly, T.; Geso, M., Potential dependent superiority of gold nanoparticles in comparison to iodinated contrast agents. Eur. J. Radiol. **2010**, *75*, 104-109.

[45] Bae, K. T., Intravenous contrast medium administration and scan timing at CT: considerations and approaches. *Radiology* **2010**, *256*, 32-61.

[46] Nadolski, G. J.; Stavropoulos, S. W., Contrast alternatives for iodinated contrast allergy and renal dysfunction: Options and limitations. J. Vasc. Surg. **2013**, *57*, 593-598.

[47] Hasebroock, K. M.; Serkova, N. J., Toxicity of MRI and CT contrast agents. *Expert Opin. Drug Metab. Toxicol.* **2009**, *5*, 403-416.

[48] Ledneva, E.; Karie, S.; Launay-Vacher, V.; Janus, N.; Deray, G., Renal safety of gadolinium-based contrast media in patients with chronic renal insufficiency. *Radiology* **2009**, *250*, 618-628.

[49] Wang, C.; Cai, X.; Zhang, J.; Wang, X.; Wang, Y.; Ge, H.; Yan, W.; Huang, Q.; Xiao, J.; Zhang, Q., Trifolium-like platinum nanoparticle-mediated photothermal therapy inhibits tumor growth and osteolysis in a bone metastasis model. *Small* **2015**, *11*, 2080-2086.

[50] Bharathiraja, S.; Bui, N. Q.; Manivasagan, P.; Moorthy, M. S.; Mondal, S.; Seo, H.; Phuoc, N. T.; Vy Phan, T. T.; Kim, H.; Lee, K. D., Multimodal tumor-homing chitosan oligosaccharide-coated biocompatible palladium nanoparticles for photo-based imaging and therapy. *Sci. Rep.* **2018**, *8*, 500.

[51] Manivasagan, P.; Bharathiraja, S.; Santha Moorthy, M.; Mondal, S.; Nguyen, T. P.; Kim, H.; Phan, T. T. V.; Lee, K. D.; Oh, J., Biocompatible chitosan

doi:10.6342/NTU202501342

oligosaccharide modified gold nanorods as highly effective photothermal agents for ablation of breast cancer cells. *Polymers* **2018**, *10*, 232.

[52] Doan, T. L.; Nguyen, H. L.; Pham, H. Q.; Pham-Tran, N. N.; Le, T. N.; Cordova, K. E., Tailoring the optical absorption of water-stable ZrIV-and HfIV-based metal-organic framework photocatalysts. *Chem. Asian J.* **2015**, *10*, 2660-2668.

[53] Yu, Y.-S.; Liang, Y.-Y.; Hsieh, C.-C.; Lin, Z.-J.; Cheng, P.-H.; Cheng, C.-C.; Chen, S.-P.; Lai, L.-J.; Wu, K. C.-W., Downsizing and soft X-ray tomography for cellular uptake of interpenetrated metal–organic frameworks. *J. Mater. Chem. B* **2024**.

[54] Chien, W.-C.; Cheng, P.-H.; Cheng, X.-J.; Chuang, C.-C.; Huang, Y.-T.; Ts, A.; Liu, C.-H.; Lu, Y.-J.; Wu, K. C.-W., MCP-1-functionalized, core–shell gold nanorod@ iron-based metal–organic framework (MCP-1/GNR@ MIL-100 (Fe)) for photothermal therapy. *ACS Appl. Mater. Interfaces* **2021**, *13*, 52092-52105.

[55] Marshall, R. J.; Griffin, S. L.; Wilson, C.; Forgan, R. S., Stereoselective Halogenation of Integral Unsaturated C-C Bonds in Chemically and Mechanically Robust Zr and Hf MOFs. *Chem. Eur. J.* **2016**, *22*, 4870-7.

[56] Marshall, R. J.; Richards, T.; Hobday, C. L.; Murphie, C. F.; Wilson, C.; Moggach, S. A.; Bennett, T. D.; Forgan, R. S., Postsynthetic bromination of UiO-66 analogues: altering linker flexibility and mechanical compliance. *Dalton Trans.* **2016**, *45*, 4132-4135.

[57] Hsieh, C.-C.; Lin, Z.-J.; Lai, L.-J., Construction of low humidity biosafety level-2 laboratory for cryo-sample environment for soft x-ray tomography imaging at Taiwan photon source. *AIP Conf. Proc.* **2023**, *2990*.

[58] Koga, H.; Selvendiran, K.; Sivakumar, R.; Yoshida, T.; Torimura, T.; Ueno, T.; Sata, M., PPARγ potentiates anticancer effects of gemcitabine on human pancreatic cancer cells. *Int. J. Oncol.* **2012**, *40*, 679-685.

[59] Yu, Y.-S.; Liang, Y.-Y.; Hsieh, C.-C.; Lin, Z.-J.; Cheng, P.-H.; Cheng, C.-C.; Chen, S.-P.; Lai, L.-J.; Wu, K. C. W., Downsizing and soft X-ray tomography for cellular uptake of interpenetrated metal–organic frameworks. *J. Mater. Chem. B* **2024**, *12*, 6079-6090.

[60] Marshall, R. J.; Griffin, S. L.; Wilson, C.; Forgan, R. S., Single-Crystal to Single-Crystal Mechanical Contraction of Metal–Organic Frameworks through Stereoselective Postsynthetic Bromination. *J. Mater. Chem. B* **2015**, *137*, 9527-9530.

[61] Dolai, J.; Mandal, K.; Jana, N. R., Nanoparticle size effects in biomedical applications. *ACS Appl. Nano Mater.* **2021**, *4*, 6471-6496.

[62] Brown, S.; Bailey, D. L.; Willowson, K.; Baldock, C., Investigation of the relationship between linear attenuation coefficients and CT Hounsfield units using radionuclides for SPECT. *Appl. Radiat. Isot.* **2008**, *66*, 1206-1212.

doi:10.6342/NTU202501342

[63] Loomis, K.; McNeeley, K.; Bellamkonda, R. V., Nanoparticles with targeting, triggered release, and imaging functionality for cancer applications. *Soft Matter* **2011**, *7*, 839-856.

[64] Yoo, J.-W.; Chambers, E.; Mitragotri, S., Factors that control the circulation time of nanoparticles in blood: challenges, solutions and future prospects. *Curr. Pharm. Des.* **2010**, *16*, 2298-2307.

[65] Sun, Z.; Zhao, Y.; Li, Z.; Cui, H.; Zhou, Y.; Li, W.; Tao, W.; Zhang, H.; Wang, H.; Chu, P. K., As an efficient contrast agent for in vivo photoacoustic imaging of cancer. *Small* **2017**, *13*, 10.1002.

[66] Mantri, Y.; Jokerst, J. V., Engineering plasmonic nanoparticles for enhanced photoacoustic imaging. *ACS Nano* **2020**, *14*, 9408-9422.

[67] Liu, D.; Lu, K.; Poon, C.; Lin, W., Metal–organic frameworks as sensory materials and imaging agents. *Inorg. Chem.* **2014**, *53*, 1916-1924.

[68] Bulte, J. W.; Kraitchman, D. L., Iron oxide MR contrast agents for molecular and cellular imaging. *NMR in Biomed.* **2004**, *17*, 484-499.

[69] Kim, D.; Park, S.; Lee, J. H.; Jeong, Y. Y.; Jon, S., Antibiofouling polymer-coated gold nanoparticles as a contrast agent for in vivo X-ray computed tomography imaging. *J. Am. Chem. Soc.* **2007**, *129*, 7661-7665.

[70] Furukawa, H.; Cordova, K. E.; O'Keeffe, M.; Yaghi, O. M., The chemistry and applications of metal-organic frameworks. *Science* **2013**, *341*, 1230444.

[71] Alkilany, A. M.; Murphy, C. J., Toxicity and cellular uptake of gold nanoparticles: what we have learned so far? *J. Nanopart. Res.* **2010**, *12*, 2313-2333.

[72] Chowdhury, M. A., Metal-organic frameworks for biomedical applications in drug delivery, and as MRI contrast agents. *J. Biomed. Mater. Res. Part A* **2017**, *105*, 1184-1194.

[73] Wang, G. D.; Chen, H.; Tang, W.; Lee, D.; Xie, J., Gd and Eu co-doped nanoscale metal–organic framework as a T1–T2 dual-modal contrast agent for magnetic resonance imaging. *Tomography* **2016**, *2*, 179.

[74] DeKrafft, K. E.; Boyle, W. S.; Burk, L. M.; Zhou, O. Z.; Lin, W., Zr-and Hf-based nanoscale metal–organic frameworks as contrast agents for computed tomography. *J. Mater. Chem.* **2012**, *22*, 18139-18144.

[75] Rieter, W. J.; Taylor, K. M.; An, H.; Lin, W.; Lin, W., Nanoscale metal− organic frameworks as potential multimodal contrast enhancing agents. *J. Am. Chem. Soc.* **2006**, *128*, 9024-9025.

[76] Tian, C.; Zhu, L.; Lin, F.; Boyes, S. G., Poly (acrylic acid) bridged gadolinium metal–organic framework–gold nanoparticle composites as contrast agents for computed tomography and magnetic resonance bimodal imaging. *ACS Appl. Mater. Interfaces* **2015**, *7*, 17765-17775.

doi:10.6342/NTU202501342

[77] Gielen, J. L.; De Schepper, A. M.; Vanhoenacker, F.; Parizel, P. M.; Wang, X. L.; Sciot, R.; Weyler, J., Accuracy of MRI in characterization of soft tissue tumors and tumor-like lesions. A prospective study in 548 patients. *Eur. Radio.* **2004**, *14*, 2320-2330.

[78] Gong, T.; Li, Y.; Lv, B.; Wang, H.; Liu, Y.; Yang, W.; Wu, Y.; Jiang, X.; Gao, H.; Zheng, X., Full-process radiosensitization based on nanoscale metal–organic frameworks. *ACS Nano* **2020**, *14*, 3032-3040.

[79] Liu, Y.; Li, J.; Chen, M.; Chen, X.; Zheng, N., Palladium-based nanomaterials for cancer imaging and therapy. *Theranostics* **2020**, *10*, 10057-10074.

[80] Hasebroock, K. M.; and Serkova, N. J., Toxicity of MRI and CT contrast agents. *Expert Opin. Drug Metab. Toxicol.* **2009**, *5*, 403-416.

[81] Kumar, P.; Anand, B.; Tsang, Y. F.; Kim, K.-H.; Khullar, S.; Wang, B., Regeneration, degradation, and toxicity effect of MOFs: Opportunities and challenges. *Environ. Res.* **2019**, *176*, 108488.

[82] Kumar, S.; Jain, S.; Nehra, M.; Dilbaghi, N.; Marrazza, G.; Kim, K.-H., Green synthesis of metal–organic frameworks: A state-of-the-art review of potential environmental and medical applications. *Coord. Chem. Rev.* **2020**, *420*, 213407.

doi:10.6342/NTU202501342

Appendix

國家衛生研究院實驗動物照護及使用委員會審查同意書
Affidavit of Approval of Animal Use Protocol
National Health Research Institutes (NHRI)

The animal use protocol listed below has been reviewed and approved by the Institutional Animal Care and Use Committee (IACUC).
以下「動物實驗計畫書」業經實驗動物照護及使用委員會審查通過.

Protocol No:	**NHRI-IACUC-113079-M1-S01**
Protocol Title：(English)	**Using photoacoustic microscopy to explore changes in the microenvironment of mouse subcutaneous tumor models after drug treatment**
(中　文)	**利用光聲顯微鏡來探究藥物治療後小鼠皮下腫瘤模型中的微環境變化**
Period of Protocol：	**Valid From： 2024/09/18 To: 2027/07/30 (yyyy/mm/dd)**
Principal Investigator (PI)：	**廖倫德 (Lun-De Liao)**
Co-PI：	

Approved Content:	Species	Amount	Housing Institute / Location / Room	Experimentation Location / Room
	Mouse	205	NHRI-LAC.	NHRI-LAC.,NHRI private lab or space for terminal experiment and animal euthanasia, Rm#R1-1116

Chair of IACUC: **Date:** 2024/12/13

備註：國家衛生研究院於111年度動物科學應用機構實地查核評比結果為「良」。

Figure A.1. Institutional animal care and use committee (IACUC): Approval Certificate

doi:10.6342/NTU202501342